CONDENSED MATTER PHYSICS

Cavity-mediated electron-electron interactions: Renormalizing Dirac states in graphene

Hang Liu[1]*, Francesco Troisi[1], Hannes Hübener[1], Simone Latini[1,2]*, Angel Rubio[1,3]*

Embedding materials in optical cavities has emerged as a strategy for tuning material properties. Here, we develop a nonperturbative quantum electrodynamical approach based on a photon-free self-consistent Hartree-Fock framework to model the coupling between cavity photons and electrons and crystals. We apply this approach to graphene coupled to cavity photons of different polarizations. Photons introduce nonlocal electron-electron interactions, solely due to the quantum nature of light, that lead to substantial renormalization of Dirac bands. The nonlocal interactions induced by anisotropic linearly polarized photons give rise to wedge-shaped bands and Dirac gap. When isotropic cavity photon modes are introduced, the Dirac cones remain gapless, but a Fermi velocity renormalization yet indicates the role of nonlocal interactions. This theoretical framework paves the way for revealing nonperturbative quantum effects in strongly coupled light-matter systems and allows for a more comprehensive discovery of cavity-induced phenomena.

INTRODUCTION

Engineering electromagnetic vacuum field fluctuations via optical cavities is emerging as a way to control the ground state of condensed matter systems (*1*–*8*). Cavity photon vacuum fluctuations have been experimentally demonstrated to control the reaction pathway of molecules by changing the potential energy landscape (*9*), affect the magneto-transport property of electron gas for tunable Landau levels and quantum Hall effects (*10*–*12*), and modify the electronic conductivity of organic and inorganic extended solids (*13*, *14*). These observations indicate that the vacuum fluctuations in optical cavities can be strong enough to mediate interactions and alter properties of quantum materials.

To understand and predict the impact of cavity vacuum fluctuations on materials, various theoretical approaches based on quantum electrodynamics (QED) have been used, with the main challenge being the modeling of cavity-mediated interactions, arising from the strong collective coupling of photons with electrons and nuclei. Photon-mediated interactions of a nonlocal type, beyond perturbation theory, are crucial for controlling atomic structures (*15*), charge transfer (*16*), chemical reactivity (*5*), and van der Waals forces (*17*) in molecules, as well as electron topology in atomic chains (*18*–*21*). These phenomena can only be grasped by approaches like Hartree-Fock (HF) approximation (*22*), coupled-cluster expansion (*16*), and exact diagonalization with partial or full configurations (*23*), which all share the capability of capturing photon-mediated nonlocal electron-electron interactions in a nonperturbative fashion. Moreover, quantum electrodynamical density functional theory (QEDFT) within the local-density approximation (*24*, *25*) provides another framework for exploring photon-mediated interactions and their consequent phenomena. It has been used for finite interacting systems, demonstrating cavity-induced donor-acceptor charge transfer (*26*) and spin glass behavior (*27*) in molecular clusters. The QEDFT is nonperturbative by construction; however, its functionals have not yet included nonlocal interactions. The present work can serve a guide to develop and improve QEDFT functionals in the future.

For extended crystalline systems, theoretical studies rely on a local approximation of cavity-induced interactions, and they are built on perturbative approximations (except for those using QEDFT) (*28*, *29*). Within perturbation theory, for example, the possibility of cavity-engineered topological phase transitions has been proposed in Su-Schrieffer-Heeger chains (*30*), graphene (*31*–*34*), and twisted layered materials (*35*, *36*). Also, modifications of superconducting properties in crystals have been explored using both perturbation theories (*37*–*40*) and nonperturbative QEDFT simulations (*41*). In the latter case, a local density approximation is used for the exchange-correlation functional, and therefore, if photon-mediated nonlocal interactions are to be included, then a different approach has to be devised.

Here, we develop a theoretical approach that addresses the coupling between optical cavities and extended crystals in a nonperturbative manner, enabling a precise description of photon-mediated nonlocal (long-range) electron interactions that arise from the quantum nature of cavity photons and have no counterparts for classical light fields. By making a high-frequency expansion of the exact QED Hamiltonian, we arrive at a photon-free Hamiltonian which features both local and nonlocal cavity-mediated electron interactions. It is important to stress that the nonlocal electron-electron interactions are not mediated by the Coulomb potential, but they result from the quantum vacuum fluctuations of the cavity photons. To solve the photon-free Hamiltonian, we perform the HF approximation on this photon-mediated interaction, arriving at what we call the photon-free QED-HF formulation, which is notably distinct from the HF method for Coulomb interactions. The direct and exchange interactions in the QED-HF formulation describe a kind of nonlocal electron-electron interaction, induced by fluctuating cavity photons, which should not be confused with that in the usual HF theory for the Coulomb electron-electron interactions. The photon-mediated nonlocal interactions arise even in a system of noninteracting electrons, where the coupling between electrons is mediated by the transverse part of the cavity vacuum field fluctuations.

With the photon-free QED-HF formulation, we investigate graphene coupled with various types of cavity electromagnetic fields

[1]Max Planck Institute for the Structure and Dynamics of Matter and Center for Free-Electron Laser Science, Luruper Chaussee 149, 22761, Hamburg, Germany. [2]Department of Physics, Technical University of Denmark, 2800 Kgs. Lyngby, Denmark. [3]Initiative for Computational Catalysis, The Flatiron Institute, 162 Fifth Avenue, New York, NY 10010, USA.
*Corresponding author. Email: hang.liu@mpsd.mpg.de (H.L.); simola@dtu.dk (S.L.); angel.rubio@mpsd.mpg.de (A.R.)

and find a substantial renormalization of Dirac electronic states. Our results show that the photon-mediated interactions induce a topologically nontrivial Dirac gap in graphene for a circularly polarized cavity photon mode and a trivial Dirac gap with a wedge-shaped band feature for a linearly polarized mode, as illustrated in Fig. 1, with the latter arising purely from the photon-induced nonlocal interactions. The gap opening from a circularly polarized mode, originating from time-reversal symmetry breaking, has a classical analog (*42*, *43*), while the gap opening from a linearly polarized mode is a result of the anisotropic long-range interactions and is a pure quantum effect induced by the cavity. This demonstrates a key difference in the phenomenology of cavity materials engineering versus Floquet engineering (*7*, *28*). When two cavity photon modes are present, all symmetries of intrinsic graphene can be restored, resulting in a gapless Dirac state with a modified Fermi velocity. Moreover, by tuning the mode polarization, amplitude, and frequency, the Dirac cones in graphene can be flexibly renormalized, establishing material symmetry engineering via optical cavities as a powerful tool for the manipulation of electronic band structure and its topology. The developed QED-HF theoretical framework is general and can be implemented as a first-principles method. Hence, it is applicable to a wide range of materials and cavity configurations and therefore opens the way to accurately model the electronic structure of materials strongly coupled to quantum vacuum field fluctuations without biasing the results through perturbative expansions.

RESULTS

Nonperturbative theory for interacting electrons and photons

Here, we present the theoretical framework for the nonperturbative modeling of an electronic system interacting with the fluctuating photons in a cavity. As discussed below, the framework is built using a HF approach and relies on a photon-free QED treatment of the light-matter coupled problem.

Photon-free QED Hamiltonian

For a system of N_e (nonrelativistic) electrons interacting with the electromagnetic field confined by a cavity, the minimal coupling prescription in Coulomb gauge together with an effective cavity photon mode description in the long-wavelength approximation (*44*) results in the following Pauli-Fierz QED Hamiltonian (*45*)

$$\hat{H} = \sum_i^{N_e} \left[\frac{(\hat{\mathbf{p}}_i - q\hat{\mathbf{A}})^2}{2m} + \hat{V}(\mathbf{r}_i) \right] + \hbar\omega\left(\frac{1}{2} + \hat{a}^\dagger\hat{a}\right) \tag{1}$$

where $\hat{\mathbf{p}}_i = -i\hbar\nabla_{\mathbf{r}_i}$ is the momentum operator for the electrons (with electron charge $q = -|e|$ and mass m), and $\hat{\mathbf{A}} = A_0(\hat{a}^\dagger\mathbf{e}^* + \hat{a}\mathbf{e})$ is the effective electromagnetic vector potential operator with mode amplitude A_0 and polarization vector $\mathbf{e}$, and ω is the cavity mode frequency. Physically, the Hamiltonian consists of three parts: the bare electron part $\hat{H}_e = \sum_i^{N_e} \hat{h}_e(\mathbf{r}_i)$ with $\hat{h}_e(\mathbf{r}_i) = \frac{\hat{\mathbf{p}}_i^2}{2m} + \hat{V}(\mathbf{r}_i)$, the bare photon part $\hat{H}_p = \hbar\omega\left(\frac{1}{2} + \hat{a}^\dagger\hat{a}\right)$, and the electron-photon interaction part $\hat{H}_{int} = -\frac{q}{m}\sum_i^{N_e} \hat{\mathbf{p}}_i \cdot \hat{\mathbf{A}} + \frac{q^2 N_e \hat{\mathbf{A}}^2}{2m}$. The interaction part is in turn composed of a paramagnetic term with $\sum_i^{N_e} \hat{\mathbf{p}}_i \cdot \hat{\mathbf{A}}$ and a diamagnetic term with $\hat{\mathbf{A}}^2$.

The diamagnetic term can be absorbed into the bare effective photon term using the Bogoliubov transformation in Supplementary Text A, reducing the Hamiltonian in Eq. 1 to

$$\hat{H} = \hat{H}_e + \hbar\tilde{\omega}\left(\frac{1}{2} + \hat{\tilde{a}}^\dagger\hat{\tilde{a}}\right) - \frac{q}{m}\sum_i^{N_e} \hat{\mathbf{p}}_i \cdot \hat{\tilde{\mathbf{A}}} \tag{2}$$

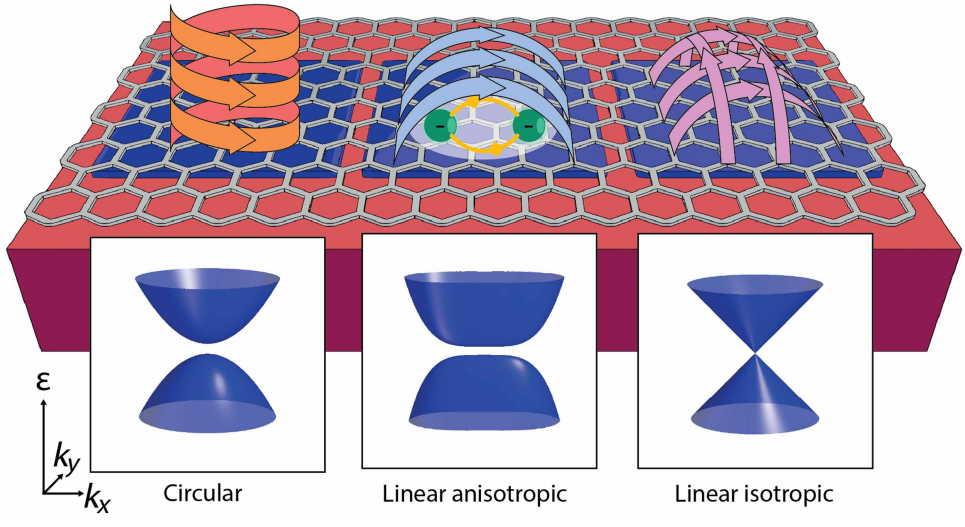

Fig. 1. Illustration of the renormalized Dirac cones of monolayer graphene coupled to cavity photon modes of different polarizations. Because of cavity-mediated electron interactions, a circularly polarized photon induces an isotropic Dirac gap with nontrivial band topology, while a linearly polarized photon induces a flat and anisotropic Dirac gap with trivial topology. In contrast, two isotropic linearly polarized photons, with the same frequency and amplitude and the perpendicular polarization directions, do not induce the Dirac gap but modify the Dirac Fermi velocity. In the setup, graphene is on the *xy* plane with $z = 0$, and *x* and *y* are along the zigzag and armchair directions of the graphene structure, respectively. k_x and k_y denote the coordinates in the two-dimensional reciprocal space of graphene, corresponding to the zigzag (*x*) and armchair (*y*) directions in real space, respectively. ε represents the energy of the QED-HF bands of graphene.

with the dressed mode frequency $\tilde{\omega}$ and vector potential operator $\hat{\tilde{\mathbf{A}}} = \tilde{A}_0(\hat{\tilde{a}}^\dagger \tilde{\mathbf{e}}^* + \hat{\tilde{a}}\tilde{\mathbf{e}})$. The polarization of the dressed mode remains the same as that of the undressed mode $\tilde{\mathbf{e}} = \mathbf{e}$. For a linearly polarized photon mode, diamagnetism renormalizes the mode frequency and amplitude to $\tilde{\omega} = \omega\sqrt{1 + \varsigma\frac{2N_e A_0^2}{\omega}}$ and $\tilde{A}_0 = A_0\frac{\sqrt{u+1}-\sqrt{u-1}}{\sqrt{2}}$ with $\varsigma = \frac{q^2}{m\hbar}$ (=1 in atomic unit) and $u = \frac{\varsigma N_e A_0^2 + \omega}{\sqrt{(2\varsigma N_e A_0^2 + \omega)\omega}}$, respectively. Differently, for a circularly polarized photon mode, diamagnetism renormalizes the mode frequency and amplitude to $\tilde{\omega} = \omega\left(1 + \varsigma\frac{N_e A_0^2}{\omega}\right)$ and $\tilde{A}_0 = A_0$, respectively.

The dressed Hamiltonian in Eq. 2 can be now represented in the dressed photon space $\{|\tilde{0}\rangle, \cdots, |\tilde{s}\rangle, \cdots\}$. Diagonal and subdiagonal matrix blocks have nonzero elements, and they satisfy $\langle\tilde{s}|\hat{\tilde{H}}|\tilde{s}\rangle = \langle\tilde{0}|\hat{\tilde{H}}|\tilde{0}\rangle + \tilde{s}\hbar\tilde{\omega}$ and $\langle\tilde{s}|\hat{\tilde{H}}|\tilde{s}+1\rangle = \sqrt{\tilde{s}+1}\,\langle\tilde{0}|\hat{\tilde{H}}|\tilde{1}\rangle$. This structure highlights that when the dressed photon frequency is much higher than the typical electronic transition frequencies taken into account, the states in different photon sectors go off resonance. As a result, the Hamiltonian matrix can be conveniently downfolded into the zero photon sector and hence remove the photonic degrees of freedom (*46*, *47*). At the first order with respect to $\frac{\tilde{A}_0^2}{\tilde{\omega}}$, the downfolding is

$$\hat{H}_{\text{eff}} = \langle\tilde{0}|\hat{\tilde{H}}|\tilde{0}\rangle - \frac{\langle\tilde{0}|\hat{\tilde{H}}|\tilde{1}\rangle\langle\tilde{1}|\hat{\tilde{H}}|\tilde{0}\rangle}{\hbar\tilde{\omega}} \tag{3}$$

where the integrals are calculated as $\langle\tilde{0}|\hat{\tilde{H}}|\tilde{0}\rangle = \hat{H}_e + \frac{\hbar\tilde{\omega}}{2}$, $\langle\tilde{0}|\hat{\tilde{H}}|\tilde{1}\rangle = -\frac{q\tilde{A}_0}{m}\sum_i^{N_e}\hat{\mathbf{p}}_i\cdot\mathbf{e}$, and $\langle\tilde{1}|\hat{\tilde{H}}|\tilde{0}\rangle = -\frac{q\tilde{A}_0}{m}\sum_i^{N_e}\hat{\mathbf{p}}_i\cdot\mathbf{e}^*$. This gives rise to the effective photon-free QED Hamiltonian

$$\hat{H}_{\text{eff}} = \hat{H}_e + \frac{\hbar\tilde{\omega}}{2} + \hat{H}_l + \hat{H}_{nl} \tag{4}$$

where

$$\hat{H}_l = -\zeta\frac{\tilde{A}_0^2}{\tilde{\omega}}\sum_i^{N_e}(\hat{\mathbf{p}}_i\cdot\mathbf{e})(\hat{\mathbf{p}}_i\cdot\mathbf{e}^*) \tag{5}$$

represents the photon-induced local single-electron interaction since it involves the momentum of the same particle i, and

$$\hat{H}_{nl} = -\zeta\frac{\tilde{A}_0^2}{\tilde{\omega}}\sum_i^{N_e}\sum_{j\neq i}^{N_e}(\hat{\mathbf{p}}_i\cdot\mathbf{e})(\hat{\mathbf{p}}_j\cdot\mathbf{e}^*) \tag{6}$$

represents the photon-induced nonlocal electron-electron interaction involving two particles i and j, and $\zeta = \frac{\varsigma}{m}$ (= 1 in atomic unit). The induced electron-electron interaction is proportional to the electron momentum, which is different from the usual Coulomb electron-electron interaction that is proportional to $\frac{1}{|\mathbf{r}_i - \mathbf{r}_j|}$. It is important to note that the photon-induced nonlocal interaction depends on the amplitude, frequency, and polarization of a photon mode, highlighting its tunable nature for controlling matter properties. In addition, as the coupled embedded material size (i.e., N_e) increases, experimental setups should target a lower bare frequency or higher bare amplitude to achieve the desired interaction strength defined by $\frac{\tilde{A}_0^2}{\tilde{\omega}}$.

This cavity-mediated electron-electron interaction is a purely quantum phenomenon arising from the transverse component of the fluctuating photon fields. This is an effect that has no counterpart with classical light. To illustrate this explicitly, we use a coherent state of light, $|\tilde{\lambda}(t)\rangle = e^{-\frac{|\tilde{\lambda}|^2}{2}}\sum_{\tilde{s}=0}^{+\infty}\frac{\tilde{\lambda}^{\tilde{s}}}{\sqrt{\tilde{s}!}}e^{-i\tilde{\omega}(\tilde{s}+\frac{1}{2})t}|\tilde{s}\rangle$ satisfying $\hat{\tilde{a}}|\tilde{\lambda}(t)\rangle = \tilde{\lambda}e^{-i\tilde{\omega}t}|\tilde{\lambda}(t)\rangle$, as a proxy of classical light. We project the electron-photon Hamiltonian in Eq. 2 onto this state, yielding

$$\langle\tilde{\lambda}(t)|\hat{\tilde{H}}|\tilde{\lambda}(t)\rangle = \hat{H}_e + \hbar\tilde{\omega}\left(\frac{1}{2} + |\tilde{\lambda}|^2\right) - \frac{q}{m}\sum_i^{N_e}\hat{\mathbf{p}}_i\cdot\tilde{\mathbf{A}}(t) \tag{7}$$

with $\tilde{\mathbf{A}}(t) = \tilde{A}_0(\tilde{\lambda}^* e^{i\tilde{\omega}t}\mathbf{e}^* + \tilde{\lambda}e^{-i\tilde{\omega}t}\mathbf{e})$. Through this projection, the vector potential operator $\hat{\tilde{\mathbf{A}}}$ acts as a classical vector potential $\tilde{\mathbf{A}}(t)$, leaving only light-mediated single electron corrections. The projected Eq. 7 is the Hamiltonian for classical time-periodic light driving in Floquet engineering (*7*).

Photon-free QED-HF formulation

To find the ground state of the many-particle Hamiltonian in Eq. 4, a HF approximation is applied to treat the photon-induced electron interactions in Eqs. 5 and 6. The electronic wave function is represented by a single Slater determinant that is constructed from the occupied single-particle orbitals $\{\varphi_i\}$ with energies $\{\varepsilon_i\}$. The orbitals can be obtained by solving the photon-free QED-HF equation (see Supplementary Text B for its derivation based on the minimization of the total energy)

$$\hat{\mathcal{F}}|\varphi_i\rangle = \varepsilon_i|\varphi_i\rangle \tag{8}$$

with the Fock operator in first quantization

$$\mathcal{F}(\hat{\mathbf{r}}) = h(\hat{\mathbf{r}}) - \sum_j^{N_e}\mathcal{J}_j(\hat{\mathbf{r}}) - \mathcal{K}_j(\hat{\mathbf{r}}) \tag{9}$$

The local part, consisting of the uncoupled electronic Hamiltonian and the operator from local interaction, is

$$h(\hat{\mathbf{r}}) = h_e(\hat{\mathbf{r}}) - \zeta\frac{\tilde{A}_0^2}{\tilde{\omega}}\hat{\Pi}_l \tag{10}$$

with $\hat{\Pi}_l = (\hat{\mathbf{p}}_\mathbf{r}\cdot\mathbf{e})(\hat{\mathbf{p}}_\mathbf{r}\cdot\mathbf{e}^*)$. The direct operator from nonlocal interaction is

$$\mathcal{J}_j(\mathbf{r})f(\mathbf{r}) = \langle\varphi_j|\zeta\frac{\tilde{A}_0^2}{\tilde{\omega}}\hat{\Pi}_{nl}|\varphi_j\rangle f(\mathbf{r}) \tag{11}$$

and the exchange operator from nonlocal interaction is

$$\mathcal{K}_j(\mathbf{r})f(\mathbf{r}) = \langle\varphi_j|\zeta\frac{\tilde{A}_0^2}{\tilde{\omega}}\hat{\Pi}_{nl}|f\rangle\varphi_j(\mathbf{r}) \tag{12}$$

with $\hat{\Pi}_{nl} = (\hat{\mathbf{p}}_\mathbf{r}\cdot\mathbf{e})(\hat{\mathbf{p}}_{\mathbf{r}'}\cdot\mathbf{e}^*) + (\hat{\mathbf{p}}_\mathbf{r}\cdot\mathbf{e}^*)(\hat{\mathbf{p}}_{\mathbf{r}'}\cdot\mathbf{e})$ for any single-particle wave function $f(\mathbf{r})$. The integral in Eqs. 11 and 12 is for coordinate $\mathbf{r}'$. Because the Fock operator depends on its eigenstates, i.e., the occupied orbitals in Eq. 8, self-consistent calculations are required. While the self-consistent HF approach has been used for finite molecules in chemistry (*22*), only the nonself-consistent perturbative HF approach has been implemented for extended crystalline systems (*33*).

With spatial periodicity, the electrons in crystals outside a cavity are described by $h_e(\mathbf{r})\varphi_{n\mathbf{k}}^0(\mathbf{r}) = \varepsilon_{n\mathbf{k}}^0\varphi_{n\mathbf{k}}^0(\mathbf{r})$, where n and $\mathbf{k}$ define the bands and crystal momenta, respectively. To numerically solve Eq. 8, the Fock operator $\hat{\mathcal{F}}$ is expressed as a

matrix, which we refer to as photon-free QED Fock matrix, in the basis set constructed from the electronic states $\{\varphi^0_{n\mathbf{k}}\}$ without interaction to cavity photons. The matrix elements $F_{n\mathbf{k}\,n'\mathbf{k}'} = \langle\varphi^0_{n\mathbf{k}}|\hat{F}|\varphi^0_{n'\mathbf{k}'}\rangle = \delta_{\mathbf{k}\mathbf{k}'}\langle\varphi^0_{n\mathbf{k}}|\hat{F}|\varphi^0_{n'\mathbf{k}}\rangle$ indicate that the matrix is diagonal in $\mathbf{k}$ space (see proof in Supplementary Text C). Thus, the QED Fock matrix can be constructed independently for each crystal momentum $\mathbf{k}$, i.e., $F_{nn'\mathbf{k}} = F_{\mathrm{l},nn'\mathbf{k}} + F_{\mathrm{nl},nn'\mathbf{k}}$. The contribution from the local operator is

$$F_{\mathrm{l},nn'\mathbf{k}} = \varepsilon^0_{n\mathbf{k}}\delta_{nn'} - \langle\varphi^0_{n\mathbf{k}}|\zeta\frac{\tilde{A}_0^2}{\tilde{\omega}}\hat{\Pi}_\mathrm{l}|\varphi^0_{n'\mathbf{k}}\rangle \tag{13}$$

and the contribution from the nonlocal operator is

$$F_{\mathrm{nl},nn'\mathbf{k}} = J_{nn'\mathbf{k}} + K_{nn'\mathbf{k}} \tag{14}$$

with the direct component

$$J_{nn'\mathbf{k}} = -\sum_{m\mathbf{k}'}^{\mathrm{occ}}\langle\varphi^0_{n\mathbf{k}}\varphi_{m\mathbf{k}'}|\zeta\frac{\tilde{A}_0^2}{\tilde{\omega}}\hat{\Pi}_\mathrm{nl}|\varphi^0_{n'\mathbf{k}}\varphi_{m\mathbf{k}'}\rangle \tag{15}$$

and the exchange component

$$K_{nn'\mathbf{k}} = \sum_{m}^{\mathrm{occ}}\langle\varphi^0_{n\mathbf{k}}\varphi_{m\mathbf{k}}|\zeta\frac{\tilde{A}_0^2}{\tilde{\omega}}\hat{\Pi}_\mathrm{nl}|\varphi_{m\mathbf{k}}\varphi^0_{n'\mathbf{k}}\rangle \tag{16}$$

where m indexes the occupied HF Bloch bands. The direct component $J_{nn'\mathbf{k}}$ accounts for the interaction of an electron with $\mathbf{k}$ to all the other electrons and itself, due to the sum of occupied orbitals for all crystal momenta $\mathbf{k}'$ in Eq. 15. In contrast, the exchange component $K_{nn'\mathbf{k}}$ accounts for the interaction of an electron with $\mathbf{k}$ to itself and the other electrons with the same crystal momentum $\mathbf{k}$, shown in Eq. 16. The self-direct and self-exchange interactions in direct and exchange components, respectively, exactly cancel with each other (see Supplementary Text B); as a result, the inclusion of both direct and exchange components guarantees the QED-HF approach to be self-interaction free.

The direct component $J_{nn'\mathbf{k}}$ is proportional to the total electron momentum $\mathbf{P} = \sum_{m\mathbf{k}'}^{\mathrm{occ}}\langle\varphi_{m\mathbf{k}'}|\hat{\mathbf{p}}_\mathbf{r}|\varphi_{m\mathbf{k}'}\rangle$ of the system. When $\mathbf{P} = 0$, the $J_{nn'\mathbf{k}}$ is zero, meaning that the Fock matrix is only contributed by the local and exchange components; thus, the Fock matrix for each crystal momentum $\mathbf{k}$ depends only on the states with the same crystal momentum $\mathbf{k}$, which allows the separate self-consistent iterations of wave functions for each $\mathbf{k}$. The resulting Fock matrix is solved and iteratively updated until convergence is reached.

In the local, direct and exchange components (Eqs. 13, 15, and 16] of the photon-free QED Fock matrix, the interaction prefactor $\frac{\tilde{A}_0^2}{\tilde{\omega}}$ scales with the number of electrons N_e, such as $\frac{\tilde{A}_0^2}{\tilde{\omega}} = \frac{A_0^2}{\omega}\left(1+\zeta\frac{2N_\mathrm{e}A_0^2}{\omega}\right)^{-1}$ and $\frac{\tilde{A}_0^2}{\tilde{\omega}} = \frac{A_0^2}{\omega}\left(1+\zeta\frac{N_\mathrm{e}A_0^2}{\omega}\right)^{-1}$ for a linearly and circularly polarized photon mode, respectively. This indicates that the modifications of electronic states by cavity fluctuating photons depend on the size of material systems.

As shown in (*44*), there is an intrinsic limit to the range over which electrons in a material are coupled to the effective cavity photon mode. Since the effective photon mode volume is finite, only the electrons within this volume should be counted in the light-matter interaction. This means that in the bulk limit (*44*), the light-matter coupling is maximized. Filling the mode volume with matter has an effect of the photon dressing from diamagnetism, which, in practice, implies that when fabricating and designing the cavity, the target frequency and amplitude of photon modes to be realized are the dressed ones. Last, compared with exact diagonalization, the photon-free QED-HF approximation is equivalent to an expansion of the electron-photon coupling problem on the ground and singly excited configuration states, as shown by the Brillouin's theorem for photon-induced electron interactions in Supplementary Text D.

The case of multiple cavity photon modes

A single effective photon mode inherently breaks the symmetry of matter by constraining the vacuum field to a single polarization. To include multiple polarizations, we allow for more cavity photon modes in the description of the light-matter interacting Hamiltonian. For a multimode cavity, the vector potential operator for $N_\mathrm{p} > 1$ photons is $\hat{\mathbf{A}} = \sum_\alpha^{N_\mathrm{p}}\hat{\mathbf{A}}_\alpha = \sum_\alpha^{N_\mathrm{p}}A_{0\alpha}(\hat{a}^\dagger_\alpha\mathbf{e}^*_\alpha + \hat{a}_\alpha\mathbf{e}_\alpha)$ with the mode index α. While the diamagnetic term resulting from this vector potential operator might mix different photons, a normal mode transformation $\hat{\mathbf{A}} = \sum_\alpha^{N_\mathrm{p}}\hat{\mathbf{A}}_\alpha \rightarrow \hat{\tilde{\mathbf{A}}} = \sum_\alpha^{N_\mathrm{p}}\hat{\tilde{\mathbf{A}}}_\alpha$ can be found (*45*), so that the multimode electron-photon Hamiltonian can be written as

$$\hat{H} = \hat{H}_\mathrm{e} + \sum_\alpha^{N_\mathrm{p}}\hbar\tilde{\omega}_\alpha\left(\frac{1}{2}+\hat{\tilde{a}}^\dagger_\alpha\hat{\tilde{a}}_\alpha\right) - \frac{q}{m}\sum_\alpha^{N_\mathrm{p}}\sum_i^{N_\mathrm{e}}\hat{\mathbf{p}}_i\cdot\hat{\tilde{\mathbf{A}}}_\alpha \tag{17}$$

with the dressed mode frequency $\tilde{\omega}_\alpha$, amplitude $\tilde{A}_{0\alpha}$, and polarization $\tilde{\mathbf{e}}_\alpha$.

A high-frequency downfolding procedure, equivalent to the one for single mode, can be applied to the multimode Hamiltonian in Eq. 17, which follows

$$\begin{aligned}\hat{H}_\mathrm{eff} = {}& \langle\tilde{0}_1,\cdots,\tilde{0}_{N_\mathrm{p}}|\hat{H}|\tilde{0}_1,\cdots,\tilde{0}_{N_\mathrm{p}}\rangle - \\ & \sum_\alpha^{N_\mathrm{p}}\left[\frac{1}{\hbar\tilde{\omega}_\alpha}\langle\tilde{0}_1,\cdots,\tilde{0}_{N_\mathrm{p}}|\hat{H}|\tilde{0}_1,\cdots,\tilde{1}_\alpha,\cdots,\tilde{0}_{N_\mathrm{p}}\rangle\cdot\right. \\ & \left.\langle\tilde{0}_1,\cdots,\tilde{1}_\alpha,\cdots,\tilde{0}_{N_\mathrm{p}}|\hat{H}|\tilde{0}_1,\cdots,\tilde{0}_{N_\mathrm{p}}\rangle\right]\end{aligned} \tag{18}$$

The multimode effective photon-free Hamiltonian is then given by

$$\hat{H}_\mathrm{eff} = \hat{H}_\mathrm{e} + \sum_\alpha^{N_\mathrm{p}}\left(\frac{\hbar\tilde{\omega}_\alpha}{2} + \hat{H}_{\mathrm{l},\alpha} + \hat{H}_{\mathrm{nl},\alpha}\right) \tag{19}$$

with $\hat{H}_{\mathrm{l},\alpha} = -\zeta\frac{\tilde{A}_{0\alpha}^2}{\tilde{\omega}_\alpha}\sum_i^{N_\mathrm{e}}(\hat{\mathbf{p}}_i\cdot\tilde{\mathbf{e}}_\alpha)(\hat{\mathbf{p}}_i\cdot\tilde{\mathbf{e}}^*_\alpha)$ and $\hat{H}_{\mathrm{nl},\alpha} = -\zeta\frac{\tilde{A}_{0\alpha}^2}{\tilde{\omega}_\alpha}\sum_i^{N_\mathrm{e}}\sum_{j\neq i}^{N_\mathrm{e}}(\hat{\mathbf{p}}_i\cdot\tilde{\mathbf{e}}_\alpha)(\hat{\mathbf{p}}_j\cdot\tilde{\mathbf{e}}^*_\alpha)$. This shows that the photon-free Hamiltonian in the case of multiple photons is a summation of the Hamiltonians corresponding to the demixed normal effective modes.

The photon-free QED-HF formulation can be directly extended to the cavities with multiple effective photon modes ($N_\mathrm{p} > 1$). The photon-free Hamiltonian in Eq. 19 features a summation of electron interactions from all the normal effective photon modes. Accordingly, the operator $\frac{\tilde{A}_0^2}{\tilde{\omega}}\hat{\Pi}_\mathrm{l}$ in Eq. 10 for a single mode should be replaced by $\sum_\alpha^{N_\mathrm{p}}\frac{\tilde{A}_{0\alpha}^2}{\tilde{\omega}_\alpha}\hat{\Pi}_{\mathrm{l},\alpha}$ with $\hat{\Pi}_{\mathrm{l},\alpha} = (\hat{\mathbf{p}}_\mathbf{r}\cdot\tilde{\mathbf{e}}_\alpha)(\hat{\mathbf{p}}_\mathbf{r}\cdot\tilde{\mathbf{e}}^*_\alpha)$, and the operator $\frac{\tilde{A}_0^2}{\tilde{\omega}}\hat{\Pi}_\mathrm{nl}$ in Eqs. 11 and 12 by $\sum_\alpha^{N_\mathrm{p}}\frac{\tilde{A}_{0\alpha}^2}{\tilde{\omega}_\alpha}\hat{\Pi}_{\mathrm{nl},\alpha}$ with $\hat{\Pi}_{\mathrm{nl},\alpha} = (\hat{\mathbf{p}}_\mathbf{r}\cdot\tilde{\mathbf{e}}_\alpha)(\hat{\mathbf{p}}_{\mathbf{r}'}\cdot\tilde{\mathbf{e}}^*_\alpha) + \hat{\Pi}_{\mathrm{nl},\alpha} = (\hat{\mathbf{p}}_\mathbf{r}\cdot\tilde{\mathbf{e}}_\alpha)(\hat{\mathbf{p}}_{\mathbf{r}'}\cdot\tilde{\mathbf{e}}^*_\alpha) + (\hat{\mathbf{p}}_\mathbf{r}\cdot\tilde{\mathbf{e}}^*_\alpha)(\hat{\mathbf{p}}_{\mathbf{r}'}\cdot\tilde{\mathbf{e}}_\alpha)$. Similar operator replacements should be applied to Eqs. 13, 15, and 16. Note that summing the interactions over multiple modes can effectively modify the interaction strength. In addition, the interaction term can vanish in certain cases. For example, this occurs when a two-dimensional material is coupled to out-of-plane polarized photon modes, as the material lacks an out-of-plane current response.

The QED-HF theoretical framework assumes cavity configurations where photon modes are dominated by the transverse component and exhibit negligible spatial variation on the scale of the matter system without resonance. However, it can be extended to include Coulomb-like direct and exchange interactions arising from the longitudinal photon component; it can also be adapted to on-resonant systems by incorporating higher-order downfolding expansions in the photon-free QED Hamiltonian. Moreover, the time-independent QED-HF framework can be adapted to model matter coupled to a driven cavity, where a dynamic Fock operator can be derived by approximating the wave function as a single time-dependent Slater determinant. When the system is time-periodic, Floquet theory can be used to eliminate the time dependence of the Fock operator and thereby get an effective QED-HF Floquet Hamiltonian, whose diagonalization yields the quasi-energy band structure of the driven system. Furthermore, the photon-free QED-HF method can be integrated into ab initio first-principles modeling packages to include the collective coupling between electrons, ions, and photons. Also, it can be extended to include correlations by combining it with QEDFT functional (*24*, *25*) while simultaneously improving the local approximation in QEDFT.

Effect of cavity-mediated nonlocal electron interactions on Dirac states in graphene

In this section, the photon-free QED-HF approach is used to study the modifications of Dirac states in graphene by cavity photons, with a specific focus on the modifications resulting from the cavity-mediated nonlocal electron-electron interaction.

The gapless Dirac states in graphene arise from the $2p_z$ orbitals of carbon atoms located at the *A* and *B* sites of a honeycomb lattice, satisfying, among others, time-reversal, spatial-inversion, and threefold rotational symmetries. Graphene is described by a tight-binding model with a nearest-neighbor (NN) hopping energy of $t_0 = -2.7$ eV (*48*), giving rise to Dirac cones with a Fermi velocity of $v_F = 0.87 \times 10^6$ m/s at $\pm\mathbf{K}$ valleys. The main ingredient to calculate the cavity-mediated electron interactions in graphene is the momentum matrix element $\mathbf{p}_{mn\mathbf{k}} = -i\hbar\langle\varphi^0_{m\mathbf{k}}|\nabla_{\mathbf{r}}|\varphi^0_{n\mathbf{k}}\rangle$ with band indexes $m, n = \{v, c\}$ for lower valence (v) and upper conduction (c) Dirac bands with crystal momentum $\mathbf{k}$, whose evaluation from the contribution of $2p_z$ orbital (*49*, *50*) is described in Supplementary Text E.

In the ground state, the charge neutral graphene interacting with cavity photon modes has total momentum $\mathbf{P} = 0$. For each crystal momentum $\mathbf{k}$, the 2×2 QED Fock matrix in the basis set $\{\varphi^0_{v\mathbf{k}}, \varphi^0_{c\mathbf{k}}\}$ is iteratively constructed by following Eqs. 13 to 16 (see its explicit form for graphene in Supplementary Text F) and solved to find the cavity-renormalized HF orbitals. The photon-free QED-HF solutions are converged to an accuracy of 10^{-12} eV in the HF energy eigenvalue.

The following subsections present the cavity-renormalized Dirac states in graphene, interacting with linearly and circularly polarized cavity photon modes, as illustrated in Fig. 1. Graphene is on the *xy* plane with $z = 0$, and *x* and *y* are along the zigzag and armchair directions of the graphene structure, respectively. The corresponding directions in reciprocal space are denoted by k_x (zigzag) and k_y (armchair) with the unit of Å^{-1}. In this section, the frequency, amplitude, and polarization of dressed effective normal photon modes are denoted as ω, A_0, and $\mathbf{e}$, respectively, without a tilde symbol (~) in the notation for brevity.

Circularly polarized photon

To describe the interaction between the electrons in graphene and a circularly polarized cavity photon mode, we set the polarization vector to $\mathbf{e} = \mathbf{e}_x + i\mathbf{e}_y$ (parallel to the graphene plane), the photon energy to $\hbar\omega = 0.3$ eV, and the amplitude to $A_0 = 2 \times 10^{-8}\frac{\text{kg}\cdot\text{m}}{\text{C}\cdot\text{s}}$, which satisfies the high-frequency condition for the photon-free QED formulation for electrons close to the Dirac points and corresponds to an experimentally accessible mode volume $V = (320\text{Å})^3$ (*32*, *51*, *52*). We find that the photon-induced local interaction opens an energy gap at the Dirac points as previously reported in literature (*31*–*34*), while the nonlocal interaction further increases the size of the gap, a quantum effect which has thus far not been discussed. As shown in Fig. 2A, the local interaction breaks the degeneracy of the Dirac point at $+\mathbf{K}$ valley, resulting in the massive Dirac cone with a band-gap $\Delta \sim 2$ meV. With the inclusion of photon-induced nonlocal interaction, the Dirac gap is enlarged to $\Delta \sim 4$ meV (Fig. 2, A and B), and the valence and conduction electrons acquire a finite isotropic effective mass. This demonstrates that the photon-induced nonlocal electron-electron interaction in Eq. 6, originating from the quantum nature of cavity photons, plays an important role in the renormalization of Dirac states in graphene and can only be captured by a non-perturbative theoretical approach.

To analyze the formation of massive Dirac cones induced by a circularly polarized cavity photon, we evaluate the electronic wave function and the change of electron density in reciprocal and real space, respectively. In the basis set $\{\varphi^0_{v\mathbf{k}}, \varphi^0_{c\mathbf{k}}\}$, the wave function of the cavity-renormalized valence Dirac band in Fig. 2B is expressed as $\varphi_{v\mathbf{k}} = c_v\varphi^0_{v\mathbf{k}} + c_c\varphi^0_{c\mathbf{k}}$ for a given crystal momentum $\mathbf{k}$. Figure 2C shows $|c_c|^2$, i.e., the component of the original conduction Dirac state $\varphi^0_{c\mathbf{k}}$ without interaction to photon. This indicates that the original valence $\varphi^0_{v\mathbf{k}}$ and conduction $\varphi^0_{c\mathbf{k}}$ states are hybridized by the circularly polarized cavity photon mode, leading to the formation of a massive Dirac cone at $+\mathbf{K}$ valley (Fig. 2, A and B). The hybridization is isotropic in reciprocal space, as expected from the symmetry of the electron-photon coupling, and it is worth mentioning that the equivalent behavior is observed for the $-\mathbf{K}$ valley.

Figure 2D shows the cavity-induced modification of the electron density, $\Delta\rho(\mathbf{r}) = \sum_{\mathbf{k}}|\varphi_{v\mathbf{k}}|^2 - |\varphi^0_{v\mathbf{k}}|^2$, contributed from the reciprocal zone $\{k_x, k_y\} \in [-1, 1]\ 10^{-3}\text{Å}^{-1}$ with respect to crystal momenta $\pm\mathbf{K}$. The zone is large enough to contain all the modified Bloch states at $\pm\mathbf{K}$ valleys for obtaining the density variation (see Supplementary Text G for the calculation details of electron density). For the $+\mathbf{K}$ valley, the density increases at *A* sites and decreases at *B* sites. Oppositely, for the $-\mathbf{K}$ valley, the density decreases at *A* sites and increases at *B* sites. As a result, the electron density from $\pm\mathbf{K}$ valleys is different $|\varphi_{v,+\mathbf{K}}(\mathbf{r})|^2 \neq |\varphi_{v,-\mathbf{K}}(\mathbf{r})|^2$, indicating that time-reversal symmetry is broken by the circularly polarized photon.

The size of the cavity-induced Dirac gap can be tuned by adjusting the amplitude and frequency of the circularly polarized photon. As shown in Fig. 2E, for a fixed photon energy, the Dirac gap becomes larger with increasing mode amplitude, following the relation $\Delta \propto A_0^2$. For a fixed mode amplitude, instead, the Dirac gap becomes smaller with increasing mode frequency and evolves as $\Delta \propto \omega^{-1}$ (Fig. 2F). The overall evolution of the gap size follows $\Delta = \kappa\frac{A_0^2}{\omega}$. Although the evolution is similar to what is predicted for the Floquet Dirac gap in graphene induced by a time-periodic circularly polarized light field (*42*, *43*), the Floquet gap is only contributed from the

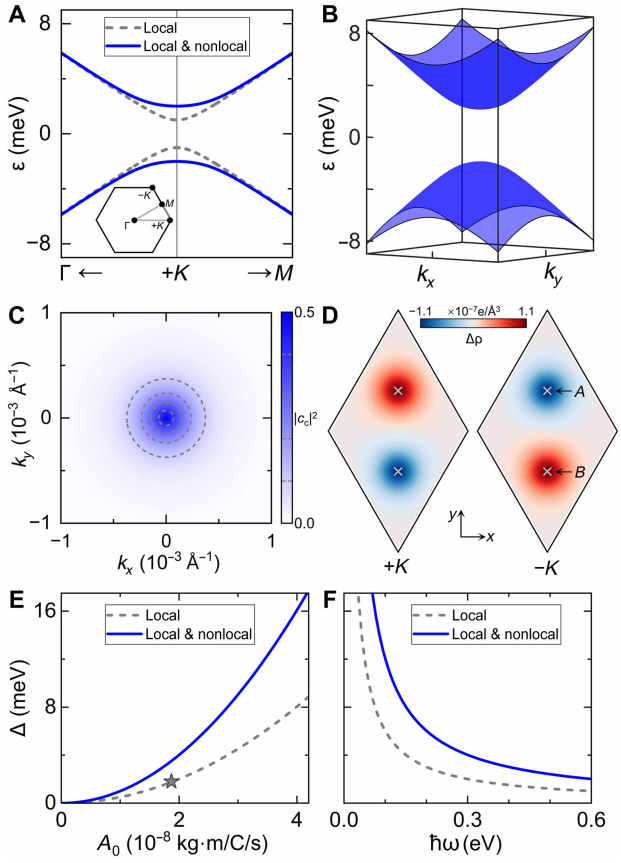

Fig. 2. Dirac states in graphene coupled with a circularly polarized photon mode. The mode has $\hbar\omega = 0.3$ eV, $A_0 = 2 \times 10^{-8} \frac{\text{kg} \cdot \text{m}}{\text{C} \cdot \text{s}}$, and $\mathbf{e} = \mathbf{e}_x + i\mathbf{e}_y$. (**A**) HF bands of the $+\mathbf{K}$ valley (inset) along $\Gamma \leftarrow +\mathbf{K} \rightarrow \mathbf{M}$ path. (**B**) Representation of the blue band in (A) in the two-dimensional reciprocal zone $\{k_x, k_y\} \in [-1, 1]\ 10^{-3}$ Å^{-1} centered at the crystal momentum $+\mathbf{K}$. (**C**) Component $|c_c|^2$ of the conduction basis state $\varphi^0_{c\mathbf{k}}$ for the lower valence band ($\varphi_{v\mathbf{k}} = c_v\varphi^0_{v\mathbf{k}} + c_c\varphi^0_{c\mathbf{k}}$) in (B). (**D**) Variation of the electron density, $\Delta\rho(\mathbf{r}) = \sum_{\mathbf{k}} |\varphi_{v\mathbf{k}}|^2 - |\varphi^0_{v\mathbf{k}}|^2$, at the specific $z = 0.33$ Å plane, where the $2p_z$ atomic orbital of carbon has its maximum. The left (right) shows the contribution to density from the $+\mathbf{K}$ ($-\mathbf{K}$) valley. The cross signs mark the position of the *A* and *B* sites. (**E** and **F**) Evolution of the Dirac bandgap in (A) as a function of the A_0 (with fixed $\hbar\omega = 0.3$ eV) and photon energy $\hbar\omega$ (with fixed $A_0 = 2 \times 10^{-8} \frac{\text{kg} \cdot \text{m}}{\text{C} \cdot \text{s}}$), respectively. The star in (E) denotes the data from perturbation approach (*32*, *34*).

local electron interaction mediated by the classical light. The dependence on the mode amplitude and frequency originates from the interaction prefactor $\frac{A_0^2}{\omega}$ in Eqs. 5 and 6, and the coefficient κ is determined by the polarization-dependent momentum matrix elements of graphene. As a sanity check, we note that the gap size is on the order of 10 meV, while the cavity photon energy is on the order of 0.3 eV; hence, the high-frequency approximation for the photon-free QED Hamiltonian in Eq. 4 is justified.

A gap size of $\Delta = 1.8$ meV, induced by a circularly polarized cavity photon with $\hbar\omega = 0.3$ eV and $A_0 = 1.87 \times 10^{-8} \frac{\text{kg} \cdot \text{m}}{\text{C} \cdot \text{s}}$, has been previously reported on the basis of perturbation theory (*31*–*34*). This is quantitatively consistent with our results for the case with only the photon-mediated local electron interaction, which demonstrates that the photon-induced nonlocal electron-electron interaction is missed in the previous perturbation modeling. Thus, the nonperturbative self-consistent photon-free QED-HF approach is necessary for the predictions of the photon-induced nonlocal interaction on the renormalization of Dirac states in graphene, as a unique quantum effect arising from cavity photons (with no counterpart for classical light, as discussed in the "Photon-free QED Hamiltonian" section).

Linearly polarized photon

For a linearly polarized photon mode, we choose the polarization $\mathbf{e} = \mathbf{e}_x$ (i.e., along the zigzag direction of graphene) and keep the photon energy $\hbar\omega = 0.3$ eV and mode amplitude $A_0 = 2 \times 10^{-8} \frac{\text{kg} \cdot \text{m}}{\text{C} \cdot \text{s}}$ as before. As shown in Fig. 3A, the photon-mediated local interaction does not break the Dirac degeneracy. In contrast, with the induced nonlocal interaction, the Dirac degeneracy is destroyed, and a bandgap of $\Delta \sim 2$ meV is formed at both $\pm\mathbf{K}$ valleys. As shown in Fig. 3B, the gapped Dirac cones are anisotropic in reciprocal space and so are the effective masses associated to the bands.

Different from the case of a circularly polarized photon where the renormalization is isotropic, the cavity-renormalized Dirac states by a linearly polarized photon are in an anisotropic superposition of valence and conduction basis states in reciprocal space. This can be quantified through the electron wave function $\varphi_{v\mathbf{k}} = c_v\varphi^0_{v\mathbf{k}} + c_c\varphi^0_{c\mathbf{k}}$ shown in Fig. 3C. Here, the conduction component $|c_c|^2$ has a butterfly shape elongated along the k_x direction in reciprocal space, indicating that threefold rotational symmetry is broken by the linearly polarized photon.

Figure 3D shows the modification of the electron density from the $\pm\mathbf{K}$ valleys, where the density variation, which is the same for the two valleys, is mainly on the $A - B$ bonds between the NN sites. The density increases on the vertical bonds and decreases on the other bonds, showing that the threefold rotational symmetry, intrinsic to the bare graphene, is broken. At the same time, the renormalized Dirac electron wave functions satisfy $|\varphi_{v,+\mathbf{K}}(\mathbf{r})|^2 = |\varphi_{v,-\mathbf{K}}(\mathbf{r})|^2$, indicating that time-reversal symmetry is not broken. In other words, the Dirac gap opening in the case of a linearly polarized cavity photon is not a consequence of time-reversal symmetry breaking and instead connected to the long-range anisotropy (characterized by threefold rotational symmetry breaking) in the presence of the photon-induced nonlocal electron-electron interaction.

In Fig. 3 (A and B), approaching $+\mathbf{K}$ along the $+\mathbf{K} - \Gamma$ direction, the renormalized Dirac bands change abruptly to become perfectly flat in the direction of the cavity polarization vector. The bands are instead shaped like a wedge. As discussed below in the section related to the effective hopping integrals, these sharp kink features are a consequence of an unphysical infinitely long-range electron-electron interaction due to the long wavelength approximation and can be prevented by truncating the interaction range. By introducing a small sublattice potential difference $V_{AB} = \pm 2 \times 10^{-5} t_0$ at *A* and *B* sites [or a weak spin-orbit coupling (SOC) strength, which would be there for realistic graphene], the bands smoothen, as shown in Fig. 3A. The long-range anisotropy from nonlocal interaction dominates the global band renormalization as in the case of $V_{AB} = 0$ (see Supplementary Text F and the section related to the effective hopping integrals).

To understand the flat-line band, we analyze the wave functions $\varphi_{v\mathbf{k}} = c_A\varphi^0_{A\mathbf{k}} + c_B\varphi^0_{B\mathbf{k}}$ for valence Dirac states in the sublattice basis set $\{\varphi^0_{A\mathbf{k}}, \varphi^0_{B\mathbf{k}}\}$ (see Supplementary Text E for the $\varphi^0_{A\mathbf{k}}$ and $\varphi^0_{B\mathbf{k}}$ functions). We specifically choose a path along k_y for $k_x = k_0 = -2\times$

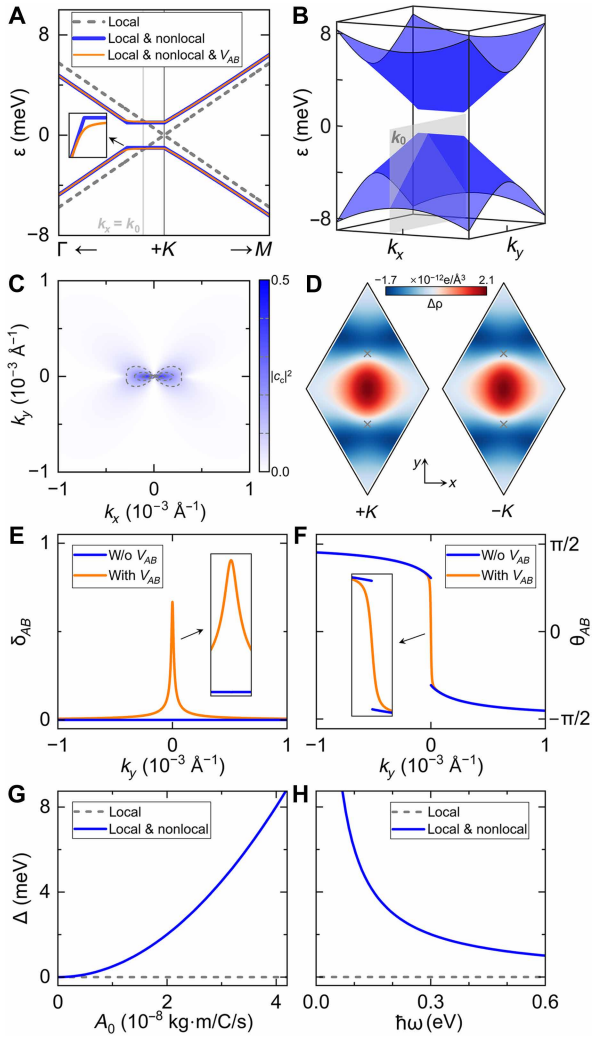

Fig. 3. Dirac states in graphene coupled with a linearly polarized photon mode. The mode has $\hbar\omega = 0.3$ eV, $A_0 = 2 \times 10^{-8} \frac{\text{kg}\cdot\text{m}}{\text{C}\cdot\text{s}}$, and $\mathbf{e} = \mathbf{e}_x$. (**A**) HF bands of the +**K** valley with and without nonlocal interaction. The former are also shown in the presence of a tiny sublattice potential value $V_{AB} = \pm 2 \times 10^{-5} t_0$. (**B**) Representation of the blue band in (A) in $\{k_x, k_y\} \in [-1, 1]\ 10^{-3}$Å^{-1} centered at +**K**. (**C**) Component $|c_c|^2$ of the conduction basis state $\varphi^0_{c\mathbf{k}}$ for the lower valence band ($\varphi_{v\mathbf{k}} = c_v\varphi^0_{v\mathbf{k}} + c_c\varphi^0_{c\mathbf{k}}$) in (B). (**D**) Variation of electron density, $\Delta\rho(\mathbf{r}) = \sum_{\mathbf{k}}|\varphi_{v\mathbf{k}}|^2 - |\varphi^0_{v\mathbf{k}}|^2$, at $z = 0.33$ Å plane for $V_{AB} = 0$. The left (right) shows the contribution from the +**K** (− **K**) valley. (**E** and **F**) The difference of wave function amplitude δ_{AB} (phase θ_{AB}) between the *A* and *B* sites for the valence states across the plane $k_x = k_0 = -2 \times 10^{-4}$ Å^{-1} [the gray plane in (B)]. Blue (orange) lines are for graphene with $V_{AB} = 0\ (\pm 2 \times 10^{-5} t_0)$. (**G** and **H**) Evolution of the Dirac bandgap in (A) as a function of A_0 (with fixed $\hbar\omega = 0.3$ eV) and $\hbar\omega$ (with fixed $A_0 = 2 \times 10^{-8} \frac{\text{kg}\cdot\text{m}}{\text{C}\cdot\text{s}}$) for $V_{AB} = 0$, respectively.

10^{-4}Å^{-1} (indicated by the gray plane in Fig. 3B). We consider both the case of zero and finite sublattice potential V_{AB}. In Fig. 3E, we plot the quantity $\delta_{AB} = |c_{A\mathbf{k}}| - |c_{B\mathbf{k}}|$, which describes the difference in the magnitudes of the wave fuction coefficients for the two lattice sites. When $V_{AB} = 0$, both sites are equivalent, i.e., $\delta_{AB} = 0$, preserving spatial inversion symmetry. Looking at the phase difference $\theta_{AB} = \text{Arg}(c_{A\mathbf{k}}) - \text{Arg}(c_{B\mathbf{k}})$ in Fig. 3F, we observe a discontinuity crossing the flat line, where a QED-HF solution cannot be found exactly at the kink and flat line. This indicates the presence of an unphysical singularity. The singularity is removed by introducing a finite V_{AB}, as evidenced by the continuous and smooth behaviors of δ_{AB} and θ_{AB} in Fig. 3 (E and F).

Last, the size of the Dirac gap, induced by a linearly polarized photon, is also tunable through adjustments of the photon parameters. As shown in Fig. 3 (G and H), with only the local interaction, the Dirac cones remain gapless regardless of the choice of photon parameters. With the nonlocal electron-electron interaction included, the Dirac gap goes again as $\Delta = \xi\frac{A_0^2}{\omega}$, but the prefactor ξ is different from that for a circularly polarized mode. Also, the length of the flat line is affected by photon parameters and evolves as $L = \chi\frac{A_0^2}{\omega}$. The direction of the singular flat line in reciprocal space corresponds to the polarization direction of the photon mode in real space and hence can be rotated in the k_xk_y plane at will by changing the mode polarization in the *xy* plane (see details in Supplementary Text H). The emergence of the singular flat-line band feature is analytically demonstrated using the two-dimensional low-energy effective Dirac model in Supplementary Text I, and also the prefactors ξ and χ for the bands evolution are analytically derived. The case of a linearly polarized cavity photon mode demonstrates that the nonperturbative QED-HF approach is essential to grasp the unique quantum effect, missed in perturbation theory, from the photon-induced nonlocal interaction in the collective electron-photon hybrid system.

Ellipticity and band topology

Here, we investigate the renormalization of Dirac states by a cavity photon as its polarization transitions from circular to linear. The elliptically polarized photon is implemented by setting the polarization vector to $\mathbf{e} = \mathbf{e}_x\cos\eta + i\mathbf{e}_y\sin\eta$ and keeping the mode frequency and amplitude as before. A circularly and linearly polarized photon mode has the ellipticity degree $\tan\eta = 1$ and 0 with the ellipticity angle $\eta = \frac{\pi}{4}$ and 0, respectively. As shown in Fig. 4A, for a single photon mode, the cavity-induced Dirac gap decreases with decreasing $\tan\eta$: With only the photon-mediated local interaction, the Dirac gap decreases to zero, whereas the gap stays finite with the nonlocal interaction included. We also note that decreasing the ellipticity degree, i.e., $\tan\eta = 1, 0.41, 0.02$ respectively with $\eta = \frac{\pi}{4}, \frac{\pi}{8}, \frac{\pi}{180}$, the Dirac dispersion becomes sharper around crystal momenta $\pm\mathbf{K}$ (Fig. 4B).

Since a circularly polarized light field can affect the band topology of Dirac states in graphene (*32*–*34*, *42*, *43*), we now discuss the evolution of the Berry curvature of cavity-renormalized Dirac bands as the ellipticity degree $\tan\eta$ goes from 1 to 0. The Berry curvature for the occupied valence Dirac band is computed, after the self-consistent QED-HF iterations, as

$$\Omega_{\mathbf{k}} = -\frac{2Im[\langle\varphi_{v\mathbf{k}}|\hat{v}_x|\varphi_{c\mathbf{k}}\rangle\langle\varphi_{c\mathbf{k}}|\hat{v}_y|\varphi_{v\mathbf{k}}\rangle]}{(\varepsilon_{c\mathbf{k}} - \varepsilon_{v\mathbf{k}})^2} \tag{20}$$

with velocity operators $\hat{v}_x = \frac{\partial\hat{\mathcal{F}}}{\partial k_x}$ and $\hat{v}_y = \frac{\partial\hat{\mathcal{F}}}{\partial k_y}$ and the photon-free QED Fock operator $\hat{\mathcal{F}}$. Figure 4C shows that, with circular polarization ($\tan\eta = 1$), the $\Omega_{\mathbf{k}}$ for the valence band is nonzero around the $\pm\mathbf{K}$ valleys. The integration of $\Omega_{\mathbf{k}}$ in the first Brillouin zone (BZ) gives rise to a finite Chern invariant $C = \frac{1}{2\pi}\int_{\text{BZ}}\Omega_{\mathbf{k}}d\mathbf{k} = 1$. This indicates that a circularly polarized photon induces a topologically nontrivial phase, which can support quantum anomalous Hall states, and is consistent with time-reversal symmetry breaking shown in the section related to circularly polarized photon modes.

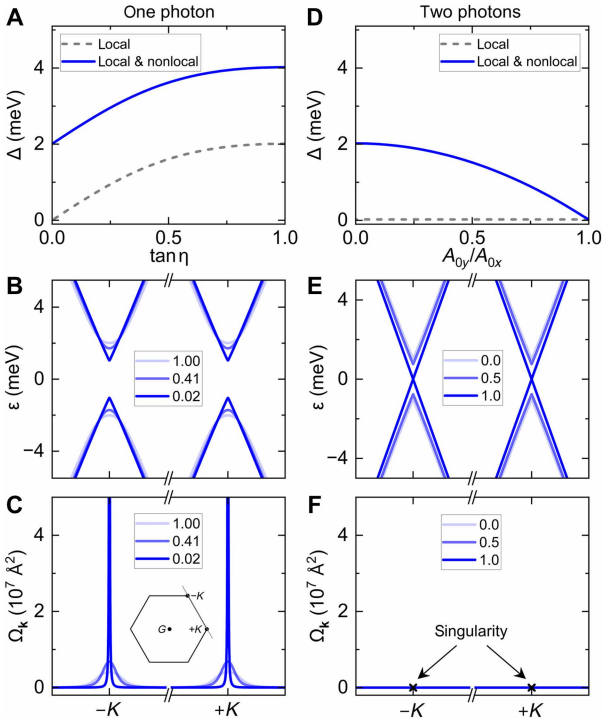

Fig. 4. Evolution of cavity-renormalized Dirac states and band topology. (**A**) Using a single photon mode with $\hbar\omega = 0.3$ eV, $A_0 = 2 \times 10^{-8}\,\frac{\text{kg}\cdot\text{m}}{\text{C}\cdot\text{s}}$, and $\mathbf{e} = \mathbf{e}_x \cos\eta + i\mathbf{e}_y \sin\eta$, the Dirac bandgap changes with mode ellipticity degree tanη. (**B**) HF bands of the $\pm\mathbf{K}$ valleys, from local and nonlocal interactions, for ellipticity degrees tanη = 1,0.41, and 0.02, corresponding to ellipticity angles $\eta = \frac{\pi}{4}, \frac{\pi}{8}$, and $\frac{\pi}{180}$, respectively. (**C**) Berry curvature for the valence band in (B). (**D**) Change of the Dirac bandgap with mode amplitude ratio $\frac{A_{0y}}{A_{0x}}$ in the presence of two linearly polarized photon modes with $\mathbf{e} = \mathbf{e}_x$ and $\mathbf{e}_y$. The photon energy of the two modes is $\hbar\omega = 0.3$ eV, and the amplitude of x-polarized mode is fixed as $A_{0x} = 2 \times 10^{-8}\,\frac{\text{kg}\cdot\text{m}}{\text{C}\cdot\text{s}}$. (**E**) HF bands of $\pm\mathbf{K}$ velleys, from local and nonlocal interactions, for the amplitude ratio $\frac{A_{0y}}{A_{0x}} = 0.0, 0.5$, and 1.0. (**F**) Berry curvature for the valence band in (E), where the cross signs indicate that the Berry curvature is singular for the valence band at the crystal momenta $\pm\mathbf{K}$.

As the ellipticity degree tanη decreases, the Berry curvature gets sharper around the crystal momenta $\pm\mathbf{K}$, as shown in Fig. 4C. The Chern number is still $C = 1$, and hence the nontrivial topology is preserved for the elliptically polarized mode. The relation $\Omega_{-\mathbf{k}} = \Omega_{+\mathbf{k}} \neq 0$ indicates the preserved spatial-inversion symmetry and broken time-reversal symmetry. In addition, the $\Omega_{\mathbf{k}}$ in two-dimensional BZ shows that the threefold rotational symmetry is broken, showing that the gap opening from the mode with $1 > \tan\eta > 0$ is also related to anisotropy in a long-range distance (accompanied with threefold rotational symmetry breaking).

For zero ellipticity degree $\tan\eta = 0$, i.e., a linearly polarized photon, the Berry curvature is zero everywhere in the BZ except on the flat-line band dispersion discussed in the section related to the linearly polarized photon, where its value cannot be calculated since the wave functions are singular. The zero Berry curvature for all the physical states indicates that the Dirac bandgap induced by a linearly polarized mode is topologically trivial.

Two linearly polarized photons: Isotropic case

Experimentally, it might be challenging to set up a cavity with a perfectly linearly polarized single photon mode, as it would require to fully suppress the mode with the other polarization direction. Hence, for a more general description, we discuss the case of two photon modes linearly polarized along the planar directions x and y. We start by considering an isotropic cavity with two degenerate linearly polarized photons with the same mode amplitude $A_0 = 2 \times 10^{-8}\,\frac{\text{kg}\cdot\text{m}}{\text{C}\cdot\text{s}}$ and the same photon energy $\hbar\omega = 0.3$ eV, as before. As shown in Fig. 5 (A and B), there is a very small difference (on the order of ~1 μeV) of energy eigenvlues in the renormalized Dirac bands when only local or both local and nonlocal interactions are included. Notably, the renormalized Dirac cones remain gapless, while the Fermi velocity is slightly modified. Along the $+\mathbf{K} \rightarrow \mathbf{M}$ paths, the Dirac Fermi velocity at the valley has the maximum variation of 0.5 per mil.

To show the effects of the two photons, we study again the wave functions and density of electrons for the renormalized Dirac cones. As shown in Fig. 5C, the original Dirac valence and conduction states hybridize with each other. Compared with that in the case of a circularly and linearly polarized photon, respectively, in Figs. 2C and 3C, the states hybridization at the $+\mathbf{K}$ valley is significantly weaker in the case of the two isotropic linearly polarized photons. Correspondingly, the renormalization of Dirac bands in Fig. 5 (A and B) is much weaker than that in the case of a circularly and linearly polarized photon, shown in Figs. 2 (A and B) and 3 (A and B), respectively.

The modification of the electron density is analyzed for the four valence states corresponding to the generic crystal momenta $-\mathbf{k}_0$, $+\mathbf{k}_0$, $+\mathbf{k}_0'$, and $+\mathbf{k}_0''$ at the $\pm\mathbf{K}$ valleys (inset in Fig. 5D). The momenta $-\mathbf{k}_0$ and $+\mathbf{k}_0$ are related by inversion symmetry, and $+\mathbf{k}_0$, $+\mathbf{k}_0'$, and $+\mathbf{k}_0''$ are connected by threefold rotational symmetry. As shown in Fig. 5D, the density variation for each of the four crystal momenta satisfies $\Delta\rho(\mathbf{r}) = \Delta\rho(-\mathbf{r})$, showing that the interacting system has spatial-inversion symmetry. At the same time, $\Delta\rho_{-\mathbf{k}_0}(\mathbf{r}) = \Delta\rho_{+\mathbf{k}_0}(\mathbf{r})$ holds, indicating that time-reversal symmetry is preserved. Furthermore, the density variation for $+\mathbf{k}_0$, $+\mathbf{k}_0'$, and $+\mathbf{k}_0''$ satisfies $\Delta\rho_{+\mathbf{k}_0}(\mathbf{r}) = \Delta\rho_{+\mathbf{k}_0'}(\hat{C}_3\mathbf{r}) = \Delta\rho_{+\mathbf{k}_0''}(\hat{C}_3\hat{C}_3\mathbf{r})$, with $\hat{C}_3$ threefold rotational operator, showing that the interacting system is threefold rotation symmetric. Thus, the two isotropic linearly polarized photons do not break the symmetries of graphene, and consequently, the Dirac cones in the electron-photon interacting system remain gapless, while the Fermi velocity is modified. In Supplementary Text I, the analytical QED-HF solutions also suggest that the Dirac cones remain gapless for graphene interacting with two isotropic linearly polarized photons.

By changing the amplitude and frequency of the two linearly polarized photon modes, the renormalization of the Dirac Fermi velocity can be modified. As shown in Fig. 5 (E and F), for a fixed photon energy $\hbar\omega = 0.3$ eV, the Fermi velocity increases with the mode amplitude; with fixed mode amplitude $A_0 = 2 \times 10^{-8}\,\frac{\text{kg}\cdot\text{m}}{\text{C}\cdot\text{s}}$, instead, the Fermi velocity decreases with increasing frequency. This shows the variation of the Dirac Fermi velocity follows the relation $|\Delta v_F| = \tau\frac{A_0^2}{\omega}$, where τ is determined by the momentum elements of graphene. If only local interaction is included, then no changes in the Dirac Fermi velocity are observed.

Two linearly polarized photons: Anisotropic case

We now study the evolution of the Dirac states in graphene when changing the two linearly polarized photon modes from isotropic to anisotropic. For the two modes, the photon energy is fixed to be the same as before; the amplitude of the x mode is fixed as $A_{0x} = 2 \times 10^{-8}\,\frac{\text{kg}\cdot\text{m}}{\text{C}\cdot\text{s}}$, while the amplitude of the y mode is tuned

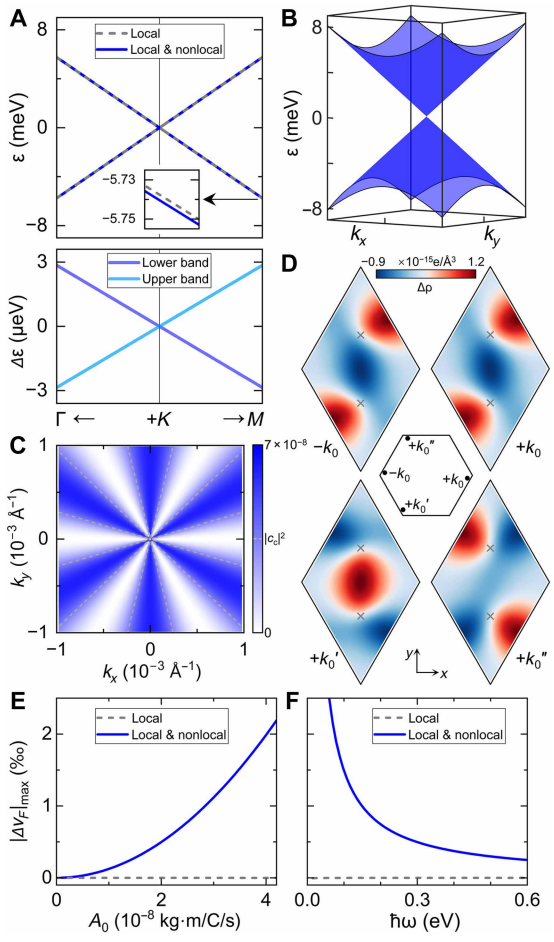

Fig. 5. Dirac states in graphene coupled with two isotropic linearly polarized photon modes. The two modes have the same $\hbar\omega = 0.3$ eV and $A_0 = 2 \times 10^{-8} \frac{\text{kg}\cdot\text{m}}{\text{C}\cdot\text{s}}$, but the perpendicular polarization vectors $\mathbf{e} = \mathbf{e}_x$ and $\mathbf{e}_y$. (**A**) HF bands for the $+\mathbf{K}$ valley. The bottom shows the variation of the bands due to addition of the nonlocal interaction. (**B**) Representation of the blue band in (A) in $\{k_x, k_y\} \in [-1, 1]\ 10^{-3}$ Å^{-1} centered at $+\mathbf{K}$. (**C**) Component $|c_c|^2$ of the conduction basis state $\varphi^0_{c\mathbf{k}}$ for the lower valence band ($\varphi_{v\mathbf{k}} = c_v\varphi^0_{v\mathbf{k}} + c_c\varphi^0_{c\mathbf{k}}$) in (B). (**D**) Variation of the electron density, $\Delta\rho(\mathbf{r}) = \sum_{\mathbf{k}} |\varphi_{v\mathbf{k}}|^2 - |\varphi^0_{v\mathbf{k}}|^2$, at $z = 0.33$ Å plane. The four panels show the contribution from the valence states with crystal momenta $-\mathbf{k}_0$, $+\mathbf{k}_0$, $+\mathbf{k}_0'$, and $+\mathbf{k}_0''$. $-\mathbf{k}_0$ is inversely symmetric to $+\mathbf{k}_0$, and the $+\mathbf{k}_0'$ and $+\mathbf{k}_0''$ are rotated by 120° and 240° with respect to $+\mathbf{k}_0$. (**E** and **F**) Evolution of the Fermi velocity along $+\mathbf{K} \rightarrow \mathbf{M}$ as a function of A_0 (with fixed $\hbar\omega = 0.3$ eV) and $\hbar\omega$ (with fixed $A_0 = 2 \times 10^{-8} \frac{\text{kg}\cdot\text{m}}{\text{C}\cdot\text{s}}$), respectively.

between $A_{0y} = 0$ and $A_{0y} = A_{0x}$. Such a cavity setup could be realized, for instance, in a cavity whose mirrors are made of a material with an anisotropic dielectric function. The most convenient way to represent the two cavity photon modes is by aligning them along the principal axes, which are assumed to be the perpendicular x and y directions here. Any other choice would be equivalent but would result in additional mode mixing terms in the Hamiltonian. As shown in Fig. 4D, we observe a smooth transition from the completely anisotropic case, with a Dirac bandgap $\Delta \sim 2$ meV induced by a single linearly polarized photon (Fig. 3), to the completely isotropic case, with no Dirac bandgap instead (Fig. 5). We stress once again that this behavior holds only if the photon-induced nonlocal interaction is included. In Fig. 4E, the bands along the $-\mathbf{K} \rightarrow +\mathbf{K}$ path are shown for different ratios $\frac{A_{0y}}{A_{0x}}$, evolving from the anisotropic to the isotropic case. Along with the reduction of gap size to zero, the length of the singular flat line of the Dirac bands (Fig. 3) gradually decreases to zero. The quantum effects on graphene of two anisotropic linearly polarized modes remain qualitatively the same as those in the single-mode case. Experimentally, such anisotropic photon mode configurations can be achieved using spatially anisotropic cavity designs, including Fabry-Pérot cavities with anisotropic mirror geometry or dielectric properties, split-ring resonator cavities with inherent structural anisotropy, and photonic crystal cavities (*29*, *53*–*55*).

As shown in Fig. 4F, the Berry curvature $\mathbf{\Omega}_{\mathbf{k}}$ of the valence Dirac band is zero, and it is undefined for the crystal momenta $\pm\mathbf{K}$, which shows that the Dirac gap induced by the two linearly polarized photon modes is topologically trivial regardless of the anisotropy. Note that, also for the graphene outside the cavity, the $\mathbf{\Omega}_{\mathbf{k}}$ is zero and undefined for the $\pm\mathbf{K}$. In addition, the relation $\mathbf{\Omega}_{-\mathbf{k}} = \mathbf{\Omega}_{+\mathbf{k}} = 0$ indicates that both time-reversal and spatial-inversion symmetries are preserved. The narrowing of Dirac gap is related to the recovery of isotropy (together with threefold rotational symmetry) when approaching the case of two isotropic photon modes, i.e., $\frac{A_{0y}}{A_{0x}} \rightarrow 1$.

Effective hopping integrals

In the section for the case of linearly polarized photons, we suggested that the presence of the singular flat line in the band structure of graphene coupled to a single linearly polarized photon is a symptom of the unphysical infinite-range description of the photon-induced interactions. To corroborate this claim, we here analyze the electron interactions in a real space tight-binding representation, where we map the interactions (both local and nonlocal) to hopping terms and show how a physical description of the interaction can be recovered. We compute the mediated effective electron hopping integrals by photon-induced interactions for arbitrary range as follows: The QED Fock matrix $F_{\{v,c\}\ \mathbf{k}}$ in the basis set $\{\varphi^0_{v\mathbf{k}}, \varphi^0_{c\mathbf{k}}\}$, directly obtained from the calculations in $\mathbf{k}$ space (as performed in all sections above), is transformed into $F_{\{A,B\}\ \mathbf{k}}$

$$F_{\{A,B\}\ \mathbf{k}} = \begin{bmatrix} F_{AA\ \mathbf{k}} & F_{AB\ \mathbf{k}} \\ F_{BA\ \mathbf{k}} & F_{BB\ \mathbf{k}} \end{bmatrix} \tag{21}$$

in the AB site representation with the basis set $\{\varphi^0_{A\mathbf{k}}, \varphi^0_{B\mathbf{k}}\}$, where $2p_z$ orbitals are used for the sites and the elements are constructed as $F_{IJ\ \mathbf{k}} = \sum_{\mathbf{R}} e^{i\mathbf{k}\cdot\mathbf{R}} t_{0I,\mathbf{R}J}$ with $I, J \in \{A, B\}$ and cell index $\mathbf{R}$ (see Supplementary Text E for the details of lattice structure). The effective electron hopping integrals in real space can be found from the Fourier transformation $t_{0I,\mathbf{R}J} = \frac{1}{N_{\mathbf{k}}} \sum_{\mathbf{k}} e^{-i\mathbf{k}\cdot\mathbf{R}} F_{IJ\ \mathbf{k}}$. Last, the range of the photon-induced interactions can be selected by truncating the effective hoppings in real space and performing an inverse Fourier transformation to get the QED Fock matrix in momentum space.

For the following results, we adopt the photon mode with energy of $\hbar\omega = 0.3$ eV and amplitude of $A_0 = 2 \times 10^{-7} \frac{\text{kg}\cdot\text{m}}{\text{C}\cdot\text{s}}$. The most interesting case is that of graphene coupled to a single linearly polarized photon. To aid numerical convergence, we introduced a nonsignificant sublattice potential difference $V_{AB} = \pm 0.004 t_0$ (which corresponds to a bandgap of 0.022 eV in the bare graphene); as shown later, the energy scales, affected by the range of the considered cavity-mediated interactions, are much larger than the one introduced by this sublattice potential. The schematic in Fig. 6A highlights the anisotropy at all orders of the

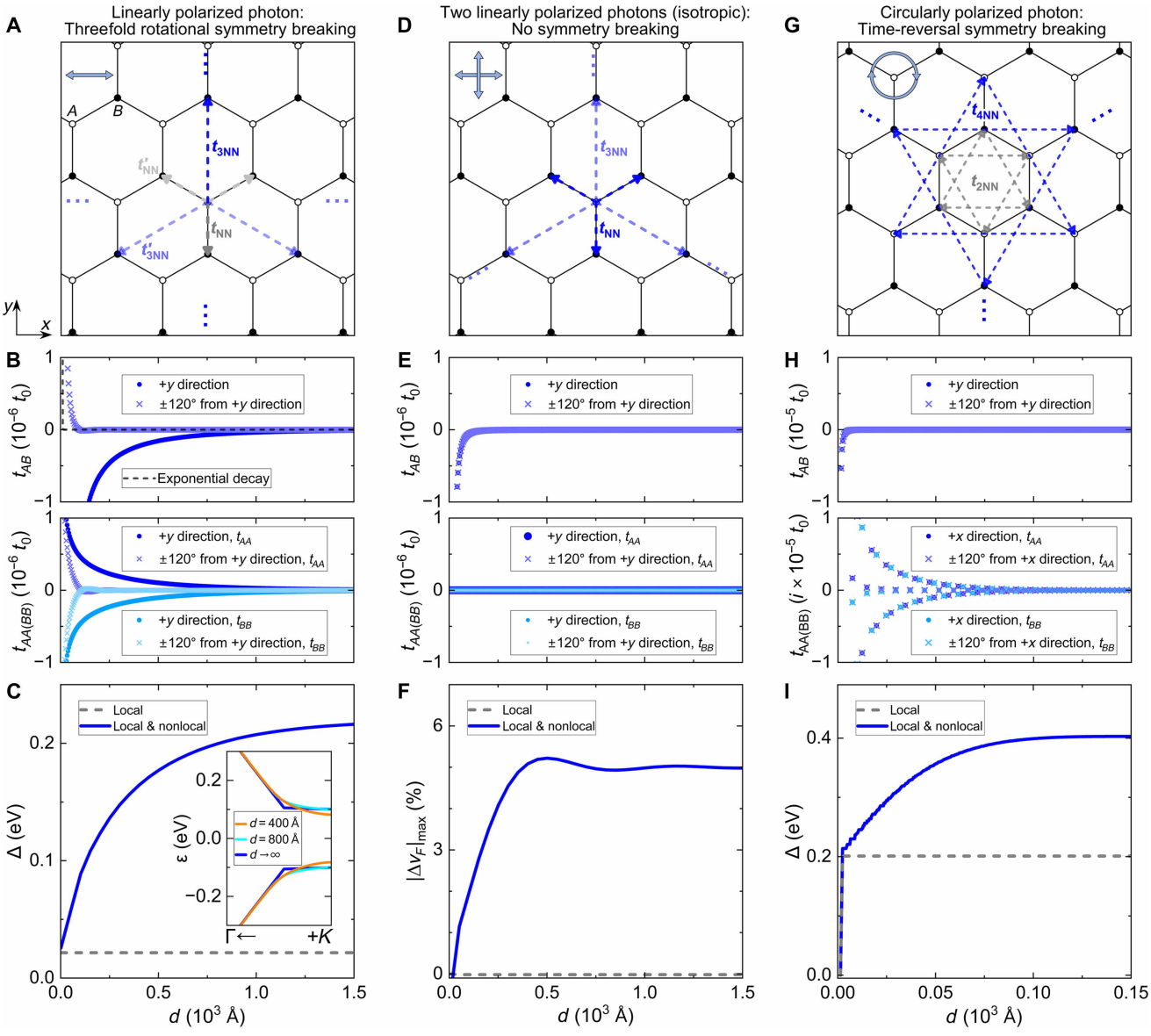

Fig. 6. Cavity-mediated effective hopping integrals in graphene. The photon energy is $\hbar\omega = 0.3$ eV, and the mode amplitude is $A_0 = 2 \times 10^{-7} \frac{\text{kg} \cdot \text{m}}{\text{C} \cdot \text{s}}$. (**A**) Schematic of hopping integrals from *A* to *B* sites, induced by a linearly polarized mode ($\mathbf{e} = \mathbf{e}_x$). Gray and light gray dashed lines show the NN integrals t_{NN} and t'_{NN}, while blue and light blue dashed lines show the third NN integrals $t_{3\text{NN}}$ and $t'_{3\text{NN}}$. (**B**) Hopping integrals, induced by a linearly polarized mode, change with distance between sites. (For numerical stability, we use a negligible $V_{AB} = \pm 0.004 t_0$). t_{AB}, t_{AA}, and t_{BB} along +*y* and directions rotated by ±120° from +*y* are shown. Hopping integrals with exponential decay in intrinsic graphene are shown. (**C**) The cavity-induced Dirac bandgap increases by including hopping integrals [in (B)] over a longer range. Inset shows the bands for truncated and infinite ranges. (**D**) Schematic of hopping integrals from *A* to *B* sites, induced by two isotropic linearly polarized modes. (**E**) Integrals t_{AB}, induced by two isotropic linearly polarized modes, change with distance between *A* and *B* sites. t_{AA} and t_{BB} remain unchanged at zero. (**F**) The cavity-renormalized Dirac Fermi velocity changes by including hopping integrals [in (E)] over a longer range. (**G**) Schematic of hopping integrals induced by a circularly polarized mode with $\mathbf{e} = \mathbf{e}_x + i\mathbf{e}_y$. Gray dashed lines show the second NN SOC-like integrals from local interaction, while blue dashed lines show long-range SOC integrals from nonlocal interaction. (**H**) Hopping integrals, induced by a circularly polarized mode, change with distance between sites. t_{AB} along +*y* and directions rotated by ±120° from +*y* are shown. SOC integrals between $A - A$ (and $B - B$) sites, along +*x* and direction rotated by ±120° from +*x*, are shown. (**I**) The cavity-induced bandgap quickly plateaus with increasing hopping range.

hopping integrals by showing that the threefold rotational symmetry of the original graphene is lost. Figure 6B shows that the change in the electron hopping integrals, when including the cavity-induced nonlocal interaction, is finite and anisotropic over a long range of distance [over hundreds of nanometers, which is comparable to characteristic cavity confinement length (*44*)]. The hoppings decay much slower with distance than the exponentially decaying ones in pristine graphene. In Supplementary Text F and the section for the linearly polarized photon, we show that while t_{AB} provides an increase of the distance between conduction and valence bands across the BZ, the modified sublattice hoppings t_{AA} and t_{BB} provide a further modification to the bands close to the $\pm\mathbf{K}$ valleys.

Cutting the range of interaction (i.e., setting the effective hopping integrals to zero for a distance larger than a given threshold) has a direct effect on the size of the Dirac gap, as shown in Fig. 6C: Long-range hopping integrals up to at least ~150 nm are needed to reach convergence on the gap size of ~0.22 eV (note that this value is significantly larger than that from the artificial sublattice potential V_{AB} used for numerical stability). Crucially, the inset in Fig. 6C demonstrates that the kinks on the flat line in bands and the singular behavior of wave functions, discussed in the section for the linearly polarized photon, are removed when the interaction range is truncated. For instance, when the interaction is truncated to a finite range $d = 800$ or 400 Å, the band kinks are removed, but the flatness of the bands in the direction of the polarization remains (Fig. 6C). This confirms that the singularity is a consequence of the infinite range of the photon-induced interactions which no realistic cavities could support.

For comparison, we performed an equivalent analysis for the case of two isotropic linearly polarized photons and the case of a single circularly polarized photon. In the presence of two isotropic linearly polarized cavity photon modes (Fig. 6, D and E), we observe a range of interaction similar to the case for a single linearly polarized photon, but as discussed in the section related to the two linearly polarized isotropic photons, because no symmetry is broken, no electronic Dirac gap is opened. Nevertheless, the renormalization of the Fermi velocity at the $\pm\mathbf{K}$ valleys shows a dependence on the interaction range (Fig. 6F). Last, for a circularly polarized photon, Fig. 6G illustrates that SOC like effective electron hoppings are induced (already at the level of cavity-induced local interactions), indicating that time-reversal symmetry is broken. Effectively, the interacting electron-photon system can be mapped to an Haldane model. The cavity-induced nonlocal interaction introduces long-range effective SOC electron hoppings (Fig. 6, H and I), up to a distance of ~10 nm which is considerably smaller than that in Fig. 6 (B and C) for a single linearly polarized mode.

DISCUSSION

In conclusion, a nonperturbative QED-HF theoretical approach based on the photon-free self-consistent framework is formulated to address the photon-mediated local and nonlocal interactions of electrons in the extended materials collectively coupled with the fluctuating photons in optical cavities. The photon-induced nonlocal electron-electron interaction, originating from the quantum nature of light confined by a cavity, naturally arises in the formulation of our photon-free QED-HF approach. Such a nonlocal interaction, quite different from the Coulomb charge-charge repulsion interaction, is properly treated through the self-consistent iterations of electronic wave functions in the coupling systems of crystalline matter and optical cavities.

Using the QED-HF approach, we have shown that photon-induced nonlocal interaction plays a crucial role in the renormalization of the Dirac electronic properties in graphene. By accounting for only the photon-mediated local interaction, a circularly polarized photon opens a topologically nontrivial Dirac gap from time-reversal symmetry breaking, while a linearly polarized photon does not lift the band degeneracy at the Dirac points. In contrast, with the photon-induced nonlocal electron-electron interaction included, both the circularly and linearly polarized photon modes open a Dirac bandgap, with nontrivial and trivial electronic topology, respectively. The formation of topologically trivial gap with flat-band dispersion is related to the anisotropy in the presence of photon-induced interaction over a long range. With two isotropic linearly polarized photons, all the symmetries in intrinsic graphene are restored, and the Dirac cones remain gapless, while the Dirac Fermi velocity is slightly affected purely by the photon-induced nonlocal interaction. We repeatedly show that the nonperturbative nature of the QED-HF approach is crucial for describing the renormalization of the Dirac electronic structure by cavity photons, demonstrating that the nonperturbative treatment is a necessity to capture the key quantum features (missed in perturbative methods, even qualitatively) resulted from the collectivity of electron-photon coupling inherent to the quantum nature of cavity photons.

In contrast to our work, previous studies on graphene embedded in a cavity (*31*–*34*) rely on perturbation theory, which, by construction, only includes photon-induced local interactions. As a result, these works overlook the quantum phenomena arising from nonlocalities. Similarly, studies on crystals other than graphene, e.g., one-dimensional and twisted layered materials (*30*, *35*, *36*), suffer from the same perturbative considerations.

Along with the renormalization of electronic bands, the optical and transport properties of Dirac states in graphene are expected to be modified. The linearity of the massless Dirac bands in pristine graphene gives rise to a universal, frequency-independent, and spatially isotropic optical conductivity σ, namely, $\mathrm{Re}[\sigma] = \frac{e^2}{4\hbar}$ (*56*). When graphene is embedded inside a cavity, the opening of an electronic gap is expected to disrupt the universal behavior of the conductivity, inducing zero conductivity within the gap. When graphene is coupled to anisotropic cavity modes, the response of the material is expected to be altered differently in the x and y directions for frequencies above the gap, hence leading to an anisotropic optical conductivity. Furthermore, in the case of circular mode polarization, the emergent nontrivial topology of the effective graphene band structure is expected to give rise to a quantized Hall conductivity and related robust topological edge states for graphene when structured to a nanoribbon form. This suggests that graphene embedded in an optical cavity could serve as a platform for developing optoelectronic and topological devices.

The cavity-induced modifications of Dirac states in graphene differ from those achieved by other material engineering approaches. For instance, applying uniaxial strain to graphene introduces anisotropy, which shifts the Dirac points in reciprocal space without the opening of an electronic gap (*57*). An topologically trivial gap can be opened by placing graphene on a substrate, via inversion symmetry breaking (*58*), but this does not result in a flat dispersion with an infinite effective mass like that induced by a linearly polarized photon in a cavity. From a microscopic point of view, the difference stems from the fact that in both strain and substrate engineering, the modifications arise from changes to the local electronic potentials, whereas cavity coupling introduces fundamentally different nonlocal effects.

The modifications in graphene proposed in this work can be probed through various experimental techniques. As highlighted above, the Dirac gap manifests as zero optical conductivity within the gap frequency range, while anisotropy from linearly polarized modes appears as directional differences in optical conductivity. Circularly polarized modes reveal nontrivial topology via quantized Hall conductivity and ballistic transport in graphene nanoribbons. In addition, the QED-HF band structure and effective mass renormalization can be observed using angle-resolved photon emission spectroscopy.

As a general theoretical framework based on wave function iterations, our photon-free QED-HF approach can be used to study a wide range of electron-photon interacting material systems that inherently have the photon-mediated electron-electron interaction over large distances due to quantum cavity confinement effects. This opens the door to predicting cavity-induced quantum phenomena in extended crystalline matter and providing deeper insights into how quantum confinement effects mediate long-range interactions and fundamentally influence material properties. For example, it would be intriguing to investigate how cavity photons modify three-dimensional Dirac states, potentially revealing phenomena distinct from those observed in graphene as a two-dimensional Dirac system, such as the transition from Dirac to Weyl fermions in three dimensions. The manipulation of transition-metal dichalcogenides and their twisted Moiré superlattices by cavity photons also presents an exciting avenue for engineering the properties associated with valley electrons and charge-ordered states.

Supplementary Materials

This PDF file includes:

Supplementary Text
Figs. S1 to S4

REFERENCES AND NOTES

1. F. J. Garcia-Vidal, C. Ciuti, T. W. Ebbesen, Manipulating matter by strong coupling to vacuum fields. *Science* **373**, eabd0336 (2021).
2. J. Bloch, A. Cavalleri, V. Galitski, M. Hafezi, A. Rubio, Strongly correlated electron-photon systems. *Nature* **606**, 41–48 (2022).
3. A. Frisk Kockum, A. Miranowicz, S. De Liberato, S. Savasta, F. Nori, Ultrastrong coupling between light and matter. *Nat. Rev. Phys.* **1**, 19–40 (2019).
4. P. Forn-Díaz, L. Lamata, E. Rico, J. Kono, E. Solano, Ultrastrong coupling regimes of light-matter interaction. *Rev. Mod. Phys.* **91**, 025005 (2019).
5. M. Hertzog, M. Wang, J. Mony, K. Börjesson, Strong light-matter interactions: A new direction within chemistry. *Chem. Soc. Rev.* **48**, 937–961 (2019).
6. T. W. Ebbesen, Hybrid light-matter states in a molecular and material science perspective. *Acc. Chem. Res.* **49**, 2403–2412 (2016).
7. H. Hübener, U. De Giovannini, C. Schäfer, J. Andberger, M. Ruggenthaler, J. Faist, A. Rubio, Engineering quantum materials with chiral optical cavities. *Nat. Mater.* **20**, 438–442 (2021).
8. M. Ruggenthaler, N. Tancogne-Dejean, J. Flick, H. Appel, A. Rubio, From a quantum-electrodynamical light-matter description to novel spectroscopies. *Nat. Rev. Chem.* **2**, 0118 (2018).
9. A. Thomas, L. Lethuillier-Karl, K. Nagarajan, R. M. A. Vergauwe, J. George, T. Chervy, A. Shalabney, E. Devaux, C. Genet, J. Moran, T. W. Ebbesen, Tilting a ground-state reactivity landscape by vibrational strong coupling. *Science* **363**, 615–619 (2019).
10. X. Li, M. Bamba, Q. Zhang, S. Fallahi, G. C. Gardner, W. Gao, M. Lou, K. Yoshioka, M. J. Manfra, J. Kono, Vacuum Bloch-Siegert shift in Landau polaritons with ultra-high cooperativity. *Nat. Photon.* **12**, 324–329 (2018).
11. G. L. Paravicini-Bagliani, F. Appugliese, E. Richter, F. Valmorra, J. Keller, M. Beck, N. Bartolo, C. Rössler, T. Ihn, K. Ensslin, C. Ciuti, G. Scalari, J. Faist, Magneto-transport controlled by Landau polariton states. *Nat. Phys.* **15**, 186–190 (2019).
12. F. Appugliese, J. Enkner, G. L. Paravicini-Bagliani, M. Beck, C. Reichl, W. Wegscheider, G. Scalari, C. Ciuti, J. Faist, Breakdown of topological protection by cavity vacuum fields in the integer quantum Hall effect. *Science* **375**, 1030–1034 (2022).
13. E. Orgiu, J. George, J. A. Hutchison, E. Devaux, J. F. Dayen, B. Doudin, F. Stellacci, C. Genet, J. Schachenmayer, C. Genes, G. Pupillo, P. Samorì, T. W. Ebbesen, Conductivity in organic semiconductors hybridized with the vacuum field. *Nat. Mater.* **14**, 1123–1129 (2015).
14. G. Jarc, S. Y. Mathengattil, A. Montanaro, F. Giusti, E. M. Rigoni, R. Sergo, F. Fassioli, S. Winnerl, S. Dal Zilio, D. Mihailovic, P. Prelovšek, M. Eckstein, D. Fausti, Cavity-mediated thermal control of metal-to-insulator transition in 1T-TaS_2. *Nature* **622**, 487–492 (2023).
15. J. Galego, F. J. Garcia-Vidal, J. Feist, Cavity-induced modifications of molecular structure in the strong-coupling regime. *Phys. Rev. X* **5**, 041022 (2015).
16. T. S. Haugland, E. Ronca, E. F. Kjønstad, A. Rubio, H. Koch, Coupled cluster theory for molecular polaritons: Changing ground and excited states. *Phys. Rev. X* **10**, 041043 (2020).
17. J. P. Philbin, T. S. Haugland, T. K. Ghosh, E. Ronca, M. Chen, P. Narang, H. Koch, Molecular van der Waals Fluids in cavity quantum electrodynamics. *J. Phys. Chem. Lett.* **14**, 8988–8993 (2023).
18. C. J. Eckhardt, G. Passetti, M. Othman, C. Karrasch, F. Cavaliere, M. A. Sentef, D. M. Kennes, Quantum Floquet engineering with an exactly solvable tight-binding chain in a cavity. *Commun. Phys.* **5**, 122 (2022).
19. D.-P. Nguyen, G. Arwas, C. Ciuti, Electron conductance and many-body marker of a cavity-embedded topological one-dimensional chain. *Phys. Rev. B* **110**, 195416 (2024).
20. D. Shaffer, M. Claassen, A. Srivastava, L. H. Santos, Entanglement and topology in Su-Schrieffer-Heeger cavity quantum electrodynamics. *Phys. Rev. B* **109**, 155160 (2024).
21. J. Li, M. Eckstein, Manipulating intertwined orders in solids with quantum light. *Phys. Rev. Lett.* **125**, 217402 (2020).
22. T. Schnappinger, D. Sidler, M. Ruggenthaler, A. Rubio, M. Kowalewski, Cavity Born-Oppenheimer Hartree-Fock Ansatz: Light-matter properties of strongly coupled molecular ensembles. *J. Phys. Chem. Lett.* **14**, 8024–8033 (2023).
23. D. Sidler, M. Ruggenthaler, H. Appel, A. Rubio, Chemistry in quantum cavities: Exact results, the impact of thermal velocities, and modified dissociation. *J. Phys. Chem. Lett.* **11**, 7525–7530 (2020).
24. C. Schäfer, F. Buchholz, M. Penz, M. Ruggenthaler, A. Rubio, Making ab initio QED functional(s): Nonperturbative and photon-free effective frameworks for strong light-matter coupling. *Proc. Natl. Acad. Sci. U.S.A.* **118**, e2110464118 (2021).
25. D. Sidler, M. Ruggenthaler, C. Schäfer, E. Ronca, A. Rubio, A perspective on ab initio modeling of polaritonic chemistry: The role of non-equilibrium effects and quantum collectivity. *J. Chem. Phys.* **156**, 230901 (2022).
26. C. Schäfer, M. Ruggenthaler, H. Appel, A. Rubio, Modification of excitation and charge transfer in cavity quantum-electrodynamical chemistry. *Proc. Natl. Acad. Sci. U.S.A.* **116**, 4883–4892 (2019).
27. D. Sidler, T. Schnappinger, A. Obzhirov, M. Ruggenthaler, M. Kowalewski, A. Rubio, Unraveling a cavity-induced molecular polarization mechanism from collective vibrational strong coupling. *J. Phys. Chem. Lett.* **15**, 5208–5214 (2024).
28. H. Hübener, E. V. Boström, M. Claassen, S. Latini, A. Rubio, Quantum materials engineering by structured cavity vacuum fluctuations. *Mater. Quant. Technol.* **4**, 023002 (2024).
29. F. Schlawin, D. M. Kennes, M. A. Sentef, Cavity quantum materials. *Appl. Phys. Rev.* **9**, 011312 (2022).
30. O. Dmytruk, M. Schirò, Controlling topological phases of matter with quantum light. *Commun. Phys.* **5**, 271 (2022).
31. O. V. Kibis, O. Kyriienko, I. A. Shelykh, Band gap in graphene induced by vacuum fluctuations. *Phys. Rev. B* **84**, 195413 (2011).
32. X. Wang, E. Ronca, M. A. Sentef, Cavity quantum electrodynamical Chern insulator: Towards light-induced quantized anomalous Hall effect in graphene. *Phys. Rev. B* **99**, 235156 (2019).
33. C. B. Dag, V. Rokaj, Engineering topology in graphene with chiral cavities. *Phys. Rev. B* **110**, L121101 (2024).
34. K. Masuki, Y. Ashida, Berry phase and topology in ultrastrongly coupled quantum light-matter systems. *Phys. Rev. B* **107**, 195104 (2023).
35. C. Jiang, M. Baggioli, Q.-D. Jiang, Engineering flat bands in twisted-bilayer graphene away from the magic angle with chiral optical cavities. *Phys. Rev. Lett.* **132**, 166901 (2024).
36. D.-P. Nguyen, G. Arwas, Z. Lin, W. Yao, C. Ciuti, Electron-photon chern number in cavity-embedded 2D Moiré materials. *Phys. Rev. Lett.* **131**, 176602 (2023).
37. F. Schlawin, A. Cavalleri, D. Jaksch, Cavity-mediated electron-photon superconductivity. *Phys. Rev. Lett.* **122**, 133602 (2019).
38. J. B. Curtis, Z. M. Raines, A. A. Allocca, M. Hafezi, V. M. Galitski, Cavity quantum Eliashberg enhancement of superconductivity. *Phys. Rev. Lett.* **122**, 167002 (2019).
39. M. A. Sentef, M. Ruggenthaler, A. Rubio, Cavity quantum-electrodynamical polaritonically enhanced electron-phonon coupling and its influence on superconductivity. *Sci. Adv.* **4**, eaau6969 (2018).
40. A. Chakraborty, F. Piazza, Long-range photon fluctuations enhance photon-mediated electron pairing and superconductivity. *Phys. Rev. Lett.* **127**, 177002 (2021).
41. I.-T. Lu, D. Shin, M. K. Svendsen, H. Hübener, U. D. Giovannini, S. Latini, M. Ruggenthaler, A. Rubio, Cavity-enhanced superconductivity in MgB_2 from first-principles quantum electrodynamics (QEDFT). *Proc. Natl. Acad. Sci. U.S.A.* **121**, e2415061121 (2024).
42. T. Oka, H. Aoki, Photovoltaic Hall effect in graphene. *Phys. Rev. B* **79**, 081406 (2009).
43. T. Kitagawa, T. Oka, A. Brataas, L. Fu, E. Demler, Transport properties of nonequilibrium systems under the application of light: Photoinduced quantum Hall insulators without Landau levels. *Phys. Rev. B* **84**, 235108 (2011).
44. M. K. Svendsen, M. Ruggenthaler, H. Hübener, C. Schäfer, M. Eckstein, A. Rubio, S. Latini, Effective equilibrium theory of quantum light-matter interaction in cavities: Extended systems and the long wavelength approximation. arXiv:2312.17374 [cond-mat.mes-hall] (2023).
45. F. H. M. Faisal, *Theory of Multiphoton Processes* (Springer, 1987).
46. S. Latini, D. Shin, S. A. Sato, C. Schaefer, U. De Giovannini, H. Huebener, A. Rubio, The ferroelectric photo ground state of $SrTiO_3$: Cavity materials engineering. *Proc. Natl. Acad. Sci. U.S.A.* **118**, e2105618118 (2021).
47. Y. Ashida, A. İmamoğlu, E. Demler, Cavity quantum electrodynamics at arbitrary light-matter coupling strengths. *Phys. Rev. Lett.* **126**, 153603 (2021).

48. S. Reich, J. Maultzsch, C. Thomsen, P. Ordejón, Tight-binding description of graphene. *Phys. Rev. B* **66**, 035412 (2002).
49. E. Malic, A. Knorr, *Graphene and Carbon Nanotubes: Ultrafast Relaxation Dynamics and Optics* (John Wiley & Sons Ltd., 2013).
50. T. G. Pedersen, K. Pedersen, T. Brun Kriestensen, Optical matrix elements in tight-binding calculations. *Phys. Rev. B* **63**, 201101 (2001).
51. H. Herzig Sheinfux, L. Orsini, M. Jung, I. Torre, M. Ceccanti, S. Marconi, R. Maniyara, D. Barcons Ruiz, A. Hötger, R. Bertini, S. Castilla, N. C. H. Hesp, E. Janzen, A. Holleitner, V. Pruneri, J. H. Edgar, G. Shvets, F. H. L. Koppens, High-quality nanocavities through multimodal confinement of hyperbolic polaritons in hexagonal boron nitride. *Nat. Mater.* **23**, 499–505 (2024).
52. X. Jin, A. Cerea, G. C. Messina, A. Rovere, R. Piccoli, F. De Donato, F. Palazon, A. Perucchi, P. Di Pietro, R. Morandotti, S. Lupi, F. De Angelis, M. Prato, A. Toma, L. Razzari, Reshaping the phonon energy landscape of nanocrystals inside a terahertz plasmonic nanocavity. *Nat. Commun.* **9**, 763 (2018).
53. G. Jarc, S. Y. Mathengattil, F. Giusti, M. Barnaba, A. Singh, A. Montanaro, F. Glerean, E. M. Rigoni, S. D. Zilio, S. Winnerl, D. Fausti, Tunable cryogenic terahertz cavity for strong light–matter coupling in complex materials. *Rev. Sci. Instrum.* **93**, 033102 (2022).
54. G. Scalari, C. Maissen, D. Turčinková, D. Hagenmüller, S. D. Liberato, C. Ciuti, C. Reichl, D. Schuh, W. Wegscheider, M. Beck, J. Faist, Ultrastrong coupling of the cyclotron transition of a 2D electron gas to a THz metamaterial. *Science* **335**, 1323–1326 (2012).
55. P. Sivarajah, A. Steinbacher, B. Dastrup, J. Lu, M. Xiang, W. Ren, S. Kamba, S. Cao, K. A. Nelson, THz-frequency magnon-phonon-polaritons in the collective strong-coupling regime. *J. Appl. Phys.* **125**, 213103 (2019).
56. A. B. Kuzmenko, E. van Heumen, F. Carbone, D. van der Marel, Universal optical conductance of graphite. *Phys. Rev. Lett.* **100**, 117401 (2008).
57. C. Si, Z. Sun, F. Liu, Strain engineering of graphene: A review. *Nanoscale* **8**, 3207–3217 (2016).
58. K. Zollner, A. W. Cummings, S. Roche, J. Fabian, Graphene on two-dimensional hexagonal BN, AlN, and GaN: Electronic, spin-orbit, and spin relaxation properties. *Phys. Rev. B* **103**, 075129 (2021).

Acknowledgments: We thank M. Ruggenthaler and I.-T. Lu for the helpful discussions. **Funding:** This work was supported by the Cluster of Excellence "CUI: Advanced Imaging of Matter"–EXC 2056–project ID 390715994, SFB-925 "Light induced dynamics and control of correlated quantum systems"–project ID 170620586 of the Deutsche Forschungsgemeinschaft (DFG), the European Research Council (ERC-2024-SyG-UnMySt–101167294), the Villum Foundation (grant no. 72146), the European Union Marie Sklodowska-Curie Doctoral Networks (TIMES, grant no. 101118915; and SPARKLE, grant no. 101169225), the Alexander von Humboldt Foundation (Humboldt Research Fellowship), and the Max Planck-New York City Center for Non-Equilibrium Quantum Phenomena. The Flatiron Institute is a division of the Simons Foundation. **Author contributions:** Conceptualization: A.R., S.L., and H.H. Methodology: H.L., F.T., H.H., S.L., and A.R. Investigation: H.L. and F.T. Visualization: H.L. and S.L. Supervision: A.R., S.L., and H.H. Writing—original draft: H.L. and S.L. Writing—review and editing: H.L., F.T., H.H., S.L., and A.R. **Competing interests:** The authors declare that they have no competing interests. **Data and materials availability:** All data needed to evaluate the conclusions in the paper are present in the paper and/or the Supplementary Materials.

Submitted 22 May 2025
Accepted 24 September 2025
Published 24 October 2025
10.1126/sciadv.adz1855